

DEEP PROBABILITY ESTIMATION

Sheng Liu^{*1} Aakash Kaku^{*1} Weicheng Zhu^{*1} Matan Leibovich^{*1} Sreyas Mohan^{*1}
 Boyang Yu¹ Laure Zanna^{1,3} Narges Razavian^{1,2} Carlos Fernandez-Granda^{1,3}

¹ NYU Center for Data Science ² NYU School of Medicine

³ Courant Institute of Mathematical Sciences

ABSTRACT

Reliable probability estimation is of crucial importance in many real-world applications where there is inherent uncertainty, such as weather forecasting, medical prognosis, or collision avoidance in autonomous vehicles. Probability-estimation models are trained on observed outcomes (e.g. whether it has rained or not, or whether a patient has died or not), because the ground-truth probabilities of the events of interest are typically unknown. The problem is therefore analogous to binary classification, with the important difference that the objective is to estimate probabilities rather than predicting the specific outcome. The goal of this work is to investigate probability estimation from high-dimensional data using deep neural networks. There exist several methods to improve the probabilities generated by these models but they mostly focus on classification problems where the probabilities are related to model uncertainty. In the case of problems with inherent uncertainty, it is challenging to evaluate performance without access to ground-truth probabilities. To address this, we build a synthetic dataset to study and compare different computable metrics. We evaluate existing methods on the synthetic data as well as on three real-world probability estimation tasks, all of which involve inherent uncertainty: precipitation forecasting from radar images, predicting cancer patient survival from histopathology images, and predicting car crashes from dashcam videos. We also give a theoretical analysis of a model for high-dimensional probability estimation which reproduces several of the phenomena evinced in our experiments. Finally, we propose a new method for probability estimation using neural networks, which modifies the training process to promote output probabilities that are consistent with empirical probabilities computed from the data. The method outperforms existing approaches on most metrics on the simulated as well as real-world data¹.

1 INTRODUCTION

We consider the problem of building models that answer questions such as: *Will it rain? Will a patient survive? Will a car collide with another vehicle?* Due to the inherently-uncertain nature of these real-world phenomena, this requires performing *probability estimation*, i.e. evaluating the likelihood of each possible outcome for the phenomenon of interest. Models for probability prediction must be trained on observed outcomes (e.g. whether it rained, a patient died, or a collision occurred), because the ground-truth probabilities are unknown. The problem is therefore analogous to binary classification, with the important difference that the objective is to estimate probabilities rather than predicting specific outcomes. In probability estimation, two identical inputs (e.g. histopathology images from cancer patients) can potentially result in two different outcomes (death vs. survival). In contrast, in classification the class label is usually completely determined by the data (a picture either shows a cat or it does not).

The goal of this work is to investigate probability estimation from high-dimensional data using deep neural networks. Deep networks trained for classification often generate probabilities, which quantify the uncertainty of the estimate (i.e. how likely the network is to classify correctly). This

^{*}Contributed equally.

¹Code and data are available at

<https://jackzhu727.github.io/deep-probability-estimation/>

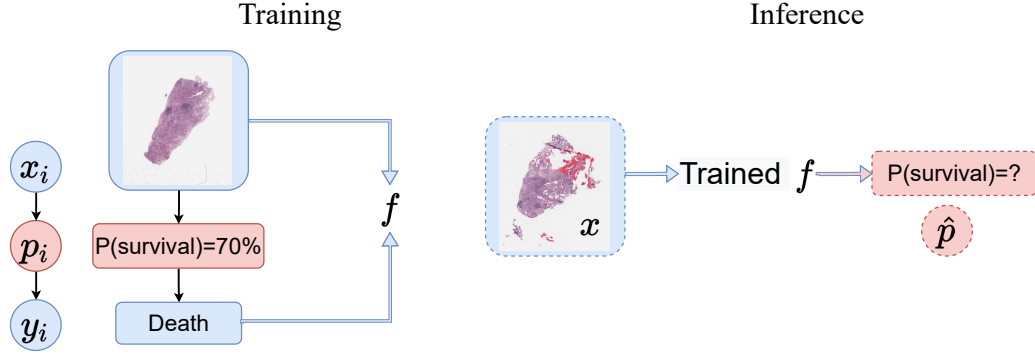


Figure 1: **The probability-estimation problem.** In probability estimation, we assume that each observed outcome y_i (e.g. death or survival in cancer patients) in the training set is randomly generated from a latent unobserved probability p_i associated to the corresponding data x_i (e.g. histopathology images). **Training** (left): Only x_i and y_i can be used for training, because p_i is not observed. **Inference** (right): Given new data x , the trained network f produces a probability estimate $\hat{p} \in [0, 1]$.

quantification has been observed to be inaccurate, and several methods have been developed to improve it (Platt, 1999; Guo et al., 2017; Szegedy et al., 2016; Zhang et al., 2020; Thulasidasan et al., 2020; Mukhoti et al., 2020; Thagaard et al., 2020), including Bayesian neural networks (Gal & Ghahramani, 2016; Wang et al., 2016; Shekhovtsov & Flach, 2019; Postels et al., 2019). However, these works restrict their attention almost exclusively to classification in datasets (e.g. CIFAR-10/100 Krizhevsky (2009), or ImageNet (Deng et al., 2009)) where the label itself is *not uncertain*: it quantifies the confidence of the model in its own prediction, *not the probability of an event of interest*. To formalize this distinction, we propose and rigorously analyze a simple high-dimensional model with *uncertain* labels, and show that even in this simple model, classification-based methods fail to yield good probability estimates.

Probability estimation from high-dimensional data is a problem of critical importance in medical prognostics (Wulczyn et al., 2020), weather prediction (Agrawal et al., 2019), and autonomous driving (Kim et al., 2019). In order to advance deep-learning methodology for probability estimation it is crucial to build appropriate benchmark datasets. Here we build a synthetic dataset and gather three real-world datasets, which we use to systematically evaluate existing methodology. In addition, we propose a novel approach for probability estimation, which outperforms current state-of-the-art methods. Our contributions are the following:

- We give a theoretical analysis of the probability estimation problem for a high-dimensional logistic model, and establish that predictors trained by minimizing the cross entropy loss overfit the observed outcomes and fail to yield calibrated outcomes. However, we show that the predictions are well calibrated during the initial stages of training.
- We introduce a new synthetic dataset for probability estimation where a population of people may have a certain disease associated with age. The task is to estimate the probability that they contract the disease from an image of their face. The data are generated using the UTKFaces dataset (Zhang et al., 2017a), which contains age information. The dataset contains multiple versions of the synthetic labels, which are generated according to different distributions designed to mimic real-world probability-prediction datasets. The dataset serves two objectives. First, it allows us to evaluate existing methodology. Second, it enables us to evaluate different metrics in a controlled scenario where we have access to ground-truth probabilities.
- We have used publicly available data to build probability-estimation benchmark datasets for three real-world applications: (1) precipitation forecasting from radar images, (2) prediction of cancer-patient survival from histopathology images, and (3) prediction of vehicle collisions from dashcam videos. We use these datasets to systematically evaluate existing approaches, which have been previously tested mainly on classification datasets.
- We propose Calibrated Probability Estimation (CaPE), a novel technique which modifies the training process so that output probabilities are consistent with empirical probabilities computed from the data. CaPE outperforms existing approaches on most metrics on synthetic and real-world data.

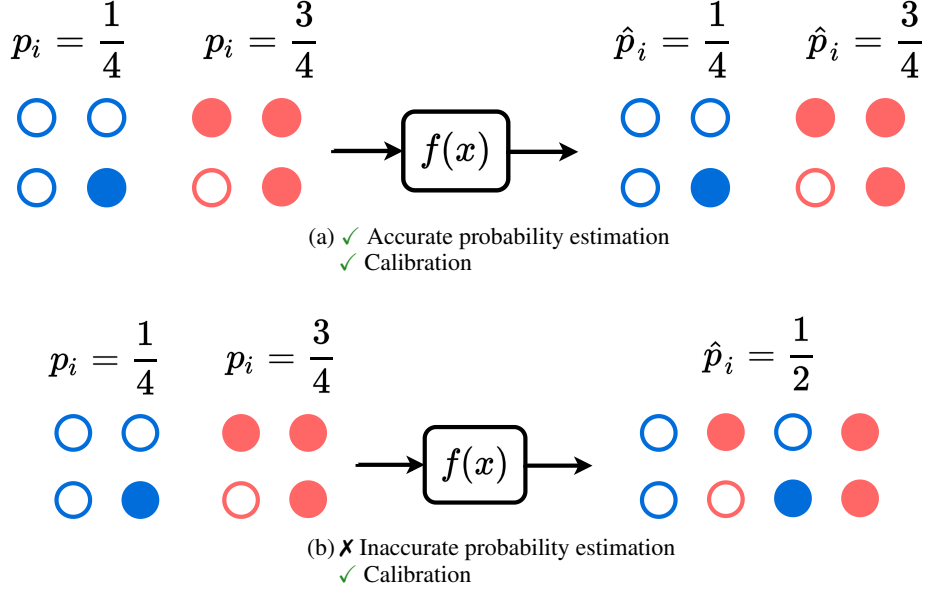


Figure 2: **Calibration is not enough.** Uncolored/colored markers denote $y = 0/1$ outcomes, respectively. Blue/red stand for two classes with different associated ground-truth probabilities ($1/4$ and $3/4$ respectively). (a) The model f retrieves the true probabilities, which requires discriminating between inputs with low and high probability. (b) The model f has no discriminative power, it just assigns the same probability to all outputs. However, the model is *perfectly calibrated* because out of all outcomes assigned 0.5 by the model, the fraction that are equal to 1 is 50% .

2 PROBLEM FORMULATION

The goal of probability estimation is to evaluate the likelihood of a certain event of interest, based on observed data. The available training data consist of n examples x_i , $1 \leq i \leq n$, each associated with a corresponding outcome y_i . In our applications of interest, the input data are high dimensional: each x_i corresponds to an image or a video. The corresponding label y_i is either 0 or 1 depending on whether or not the event in question occurred. For example, in the cancer-survival application x_i is a histopathology image of a patient, and y_i equals 1 if the patient survived for 5 years after x_i was collected. The data have inherent uncertainty: y_i , the patient’s survival, does not depend deterministically on the histopathology image (due e.g. to comorbidities and other health factors). Instead, we assume that y_i equals 1 with a certain probability p_i associated with x_i , as illustrated in Figure 1, because the input data provides key information about the patient’s survival chances.

At inference, a probability-estimation model aims to generate an estimate \hat{p} of the underlying probability p , associated with a new input data point x (e.g. the probability of survival for over 5 years for new patients based on their histopathology data). To summarize, this is not a classification problem, because the labels are not completely predictable. Instead, the goal is to predict the probability of the outcome, which is critical in choosing a course of treatment for the patient.

3 EVALUATION METRICS

Probability estimation shares similar target labels and network outputs with binary classification. However, classification accuracy is *not* an appropriate metric for evaluating probability-estimation models due to the inherent uncertainty of the outcomes. This is illustrated by the example in Figure 2a where a perfect probability estimate would result in a classification accuracy of just 75% .²

²A perfect model (in terms of probability estimation), assigns 0.25 to the blue class and 0.75 to the red class. To maximize classification accuracy, we predict 1 when the model outputs 0.75 (red examples) and 0 when it

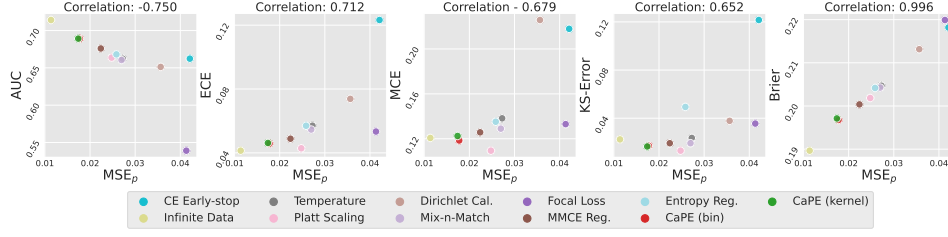


Figure 3: **Evaluating evaluation metrics.** We use synthetic data to compare different metrics to the *gold-standard* MSE_p that uses ground-truth probabilities. Brier score is highly correlated with MSE_p , in contrast to the classification metric AUC and the calibration metrics ECE, MCE and KS-Error. The graphs show the results of the proposed method CaPE, as well as the baselines described in Section 7.3 on the *Linear* scenario (see Section 7.1). Results on other scenarios and a similar comparison with KL_p are reported in Appendix F.

Metrics when ground-truth probabilities are available. For synthetic datasets, we have access to the ground truth probability labels and can use them to evaluate performance. Two reasonable metrics are the mean squared error or ℓ_2 distance MSE_p , and the Kullback–Leibler divergence KL_p between the estimated and ground-truth probabilities:

$$\text{MSE}_p = \frac{1}{N} \sum_{i=1}^N (\hat{p}_i - p_i)^2,$$

$$\text{KL}_p = \frac{1}{N} \sum_{i=1}^N \left(\hat{p}_i \log \left(\frac{\hat{p}_i}{p_i} \right) + (1 - \hat{p}_i) \log \left(\frac{1 - \hat{p}_i}{1 - p_i} \right) \right).$$

N is the number of data points, and p_i, \hat{p}_i are the ground-truth and predicted probabilities, respectively.

Calibration metrics. Ground-truth probabilities are not available for real-world data. In order to evaluate the probabilities estimated by a model, we need to compare them to the observed probabilities. To this end, we aggregate the examples for which the model output equals a certain value (e.g. 0.5), and verify what fraction of them have outcomes equal to 1. If the fraction is close to the model output, then the model is said to be well calibrated.

Definition 3.1. A model f is well *calibrated* if

$$\mathbb{P}(y = 1 \mid f(\mathbf{x}) \in I(q)) = q, \quad \forall 0 \leq q \leq 1, \quad (1)$$

where y is the observed outcome, $f(\mathbf{x})$ is the probability predicted by model f for input \mathbf{x} , and $I(q)$ is a small interval around q .

Model calibration can be evaluated using the expected calibration error (ECE) (Guo et al., 2017) (note however that the definition in Guo et al. (2017) is specific to classification). Given a probability-estimation model f and a dataset of input data \mathbf{x}_i and associated outcomes y_i , $1 \leq i \leq N$, we partition the examples into B bins, I_1, I_2, \dots, I_B , according to the probabilities assigned to the examples by the model. Let Q_1, \dots, Q_{B-1} the B -quantiles of the set $\{f(\mathbf{x}_1), \dots, f(\mathbf{x}_N)\}$, we have $I_b := [Q_{b-1}, Q_b] \cap \{f(\mathbf{x}_i)\}_{i=1}^N$ (setting $Q_0 = 0$). For each bin, we compute the mean predicted and empirical probabilities,

$$p_{\text{emp}}^{(b)} = \mathbb{E}(y \mid f(\mathbf{x}) \in I_b) = \frac{1}{|I_b|} \sum_{i \in \text{Index}(I_b)} y_i, \quad (2)$$

$$q^{(b)} = \frac{1}{|I_b|} \sum_{i \in \text{Index}(I_b)} f(\mathbf{x}_i), \quad (3)$$

where $\text{Index}(I_b) = \{i \mid f(\mathbf{x}_i) \in I_b\}$.

outputs 0.25 (blue examples). However, 25% of red examples have an outcome of 0, and 25% of blue examples have an outcome of 1. As a result, the model would only have 75% accuracy.

The pairs $(q^{(b)}, p_{\text{emp}}^{(b)})$ can be plotted as a reliability diagram, shown in the second row of Figure 4 and in Figure 6. ECE is then defined as

$$\text{ECE} = \frac{1}{B} \sum_{b=1}^B |p_{\text{emp}}^{(b)} - q^{(b)}|. \quad (4)$$

Other metrics for calibration include the maximum calibration error (MCE) defined as

$$\text{MCE} = \max_{b=1, \dots, B} |p_{\text{emp}}^{(b)} - q^{(b)}|,$$

and the Kolmogorov-Smirnov error (KS-error) (Gupta et al., 2021), a metric based on the cumulative distribution function, which is described in more detail in Appendix D.

Brier score. Crucially, a model without any discriminative power can be perfectly calibrated (see Figure 2). The Brier score is a metric designed to evaluate both calibration and discriminative power. It is the mean squared error between the predicted probability and the observed outcomes:

$$\text{Brier} = \frac{1}{N} \sum_{i=1}^N (\hat{p}_i - y_i)^2. \quad (5)$$

This score can be decomposed into two terms associated with calibration and discrimination, as shown in Appendix E. Using the synthetic data in Section 7.1, where the ground-truth probabilities are known, we show that Brier score is indeed a reliable proxy for *gold-standard* MSE metric based on ground-truth probabilities MSE_p , in contrast to calibration metrics such as ECE, MCE or KS-error, and to classification metrics such as AUC (see Figure 3 and Appendix F).

4 EARLY LEARNING AND MEMORIZATION IN PROBABILITY ESTIMATION

Prediction models based on deep learning are typically trained by minimizing the cross entropy between the model output and the training labels (Goodfellow et al., 2016). This cost function is a *proper scoring rule*, meaning it evaluates probability estimates in a consistent manner and is therefore guaranteed to be well calibrated in an infinite-data regime (Buja et al., 2005), as illustrated by Figure 4 (first column).

Unfortunately, in practice, prediction models are trained on finite data. This is crucial in the case of deep neural networks, which are highly overparametrized and therefore prone to overfitting (Goodfellow et al., 2016). For classification, deep neural networks have been shown to be capable of fitting arbitrary random labels (Zhang et al., 2017a). In probability estimation, we observe that neural networks indeed eventually overfit and *memorize* the observed outcomes completely. Moreover, the estimated probabilities collapse to 0 or 1 (Figure 4, second column), a phenomenon that has also been reported in classification (Mukhoti et al., 2020). However, calibration is preserved during the first stages of training (Figure 4, third column). This is reminiscent of the *early-learning* phenomenon observed for classification from partially corrupted labels (Yao et al., 2020; Xia et al., 2020), where neural networks learn from the correct labels before eventually overfitting the false ones (Liu et al., 2020).

Though early learning and memorization are typically observed when training prediction models based on deep neural networks, we argue that these observations represent a much more general phenomenon, intrinsic to the problem of probability estimation with finite data when the dimension is large. To substantiate this claim, we propose a simple analytical model, where data samples $\mathbf{x}_i \in \mathbb{R}^p$ are drawn from a high dimensional normal distribution $\mathbf{x}_i \sim \mathcal{N}(0, I_p)$. The probability of each data point is determined by a generalized linear model $p_i(\boldsymbol{\theta}) = (1 + e^{-\langle \boldsymbol{\theta}, \mathbf{x}_i \rangle})^{-1}$, with true parameter $\boldsymbol{\theta}^*$. For $k \geq 1$ we denote by \hat{p}^k the predictor obtained by running k iterations of gradient descent on the cross-entropy loss with step size η . We prove the following.

Theorem 4.1 (Informal). *There exists $\kappa^* \in (0, +\infty)$ such that the following holds: if p and n are sufficiently large, the mean squared error of \hat{p}^k decreases during the first $k = O(1/\eta)$ iterations of gradient descent, but if $\frac{p}{n} > \kappa^*$, then as $k \rightarrow \infty$, \hat{p}^k collapses to a predictor that only predicts probabilities 0 and 1.*

A precise statement and proof can be found in Appendix A. Theorem 4.1 indicates that even simple generalized linear models exhibit the early learning and memorization phenomena: in high dimen-

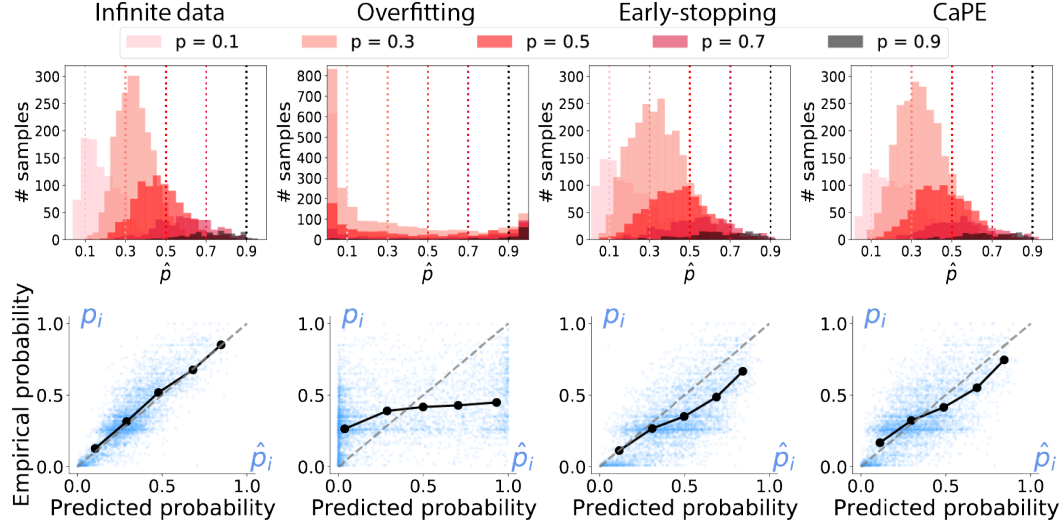


Figure 4: **Miscalibration due to overfitting and how to avoid it.** The top row shows the histogram of predicted probabilities for the synthetic *Discrete* scenario (see Section 7.1). Ideally each histogram should be concentrated around the corresponding value of p . The bottom row shows results for the *Linear* scenario. The horizontal and vertical coordinate of each blue point represent the predicted (\hat{p}_i) and true (p_i) probabilities of a test example respectively. We also show a reliability diagram of binned mean predicted and empirical probabilities in black (see Section 3). The dashed line indicates perfect calibration. When trained on *infinite data* (i.e. resampling outcome labels at each epoch according to ground-truth probabilities), models minimizing cross-entropy are well calibrated (first column). However, when trained on fixed observed outcomes, the model eventually overfits and the probabilities collapse to either 0 or 1 (second column). This is mitigated via early stopping (i.e. selecting the model based on validation cross-entropy loss), which yields relatively good calibration (third column). The proposed Calibration Probability Estimation (CaPE) method exploits this to further improve the model while ensuring that the output remains well calibrated. Appendix C.3 shows plots for all synthetic data scenarios.

sions, predictors obtained by cross-entropy minimization eventually memorize the data; however, this phenomenon does *not* occur if gradient descent is stopped early. This is illustrated in Figures 8 and 7 in Appendix B, which demonstrate that empirically the linear model has this qualitative behavior. These observations motivate our proposed methodology.

5 CALIBRATED PROBABILITY ESTIMATION (CAPE)

We propose to exploit the training dynamics of cross-entropy minimization through a method that we name *Calibrated Probability Estimation* (CaPE). Our starting point is a model obtained via early stopping using validation data on the cross-entropy loss. CaPE is designed to further improve the discrimination ability of the model, while ensuring that it remains well calibrated. This is achieved by alternatively minimizing the following two loss functions:

Discrimination loss: Cross entropy between the model output and the observed binary outcomes,

$$\mathcal{L}_D = - \sum_{i=1}^N [y_i \log(f(\mathbf{x}_i)) + (1 - y_i) \log(1 - f(\mathbf{x}_i))]$$

Calibration loss: Cross entropy between the output probability of the model and the empirical probability of the outcomes conditioned on the model output:

$$\mathcal{L}_C = - \sum_{i=1}^N [p_{\text{emp}}^i \log(f(\mathbf{x}_i)) + (1 - p_{\text{emp}}^i) \log(1 - f(\mathbf{x}_i))],$$

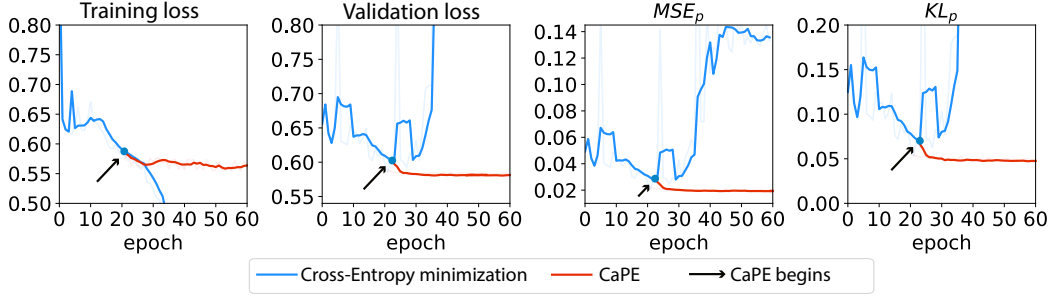


Figure 5: **Calibrated Probability Estimation prevents overfitting.** Comparison between the learning curves of cross-entropy (CE) minimization and the proposed calibrated probability estimation (CaPE), smoothed with a 5-epoch moving average. After an *early-learning* stage where both training and validation losses decrease, CE minimization overfits (first and second graph), with disastrous consequences in terms of probability estimation (third and fourth graph). In contrast, CaPE prevents overfitting, continuing to improve the model while maintaining calibration (see Figure 4).

Algorithm 1 Pseudocode for CaPE

<p>Require: f ▷ early stopped model</p> <p>Require: m ▷ freq. of training with \mathcal{L}_C</p> <p>Require: $\{\mathbf{x}_i, y_i\}_{i=1}^N$ ▷ training set</p> <p>Require: $K(p, q) := \exp[-(p - q)^2 / \sigma^2]$ ▷ Gaussian kernel</p> <p>for $t = 1$ to num_epochs do</p> <p style="padding-left: 10px;">if $t \bmod m = 0$ then</p> <p style="padding-left: 20px;">$\hat{p}_i \leftarrow f(\mathbf{x}_i), \forall i$</p> <p style="padding-left: 20px;">Update $p_{\text{emp}}^i, \forall i$, with BIN or KERNEL</p> <p style="padding-left: 20px;">$\mathcal{L} \leftarrow \mathcal{L}_C$ ▷ compute discrimination loss</p> <p style="padding-left: 10px;">else</p> <p style="padding-left: 20px;">$\mathcal{L} \leftarrow \mathcal{L}_D$ ▷ compute calibration loss</p> <p style="padding-left: 10px;">end if</p> <p style="padding-left: 10px;">$f \leftarrow \text{backprop with } \mathcal{L}$ ▷ train with loss</p> <p>end for</p>	<p>function BIN(B) ▷ B-number of bins</p> <p style="padding-left: 10px;">$I_1, \dots, I_B \leftarrow \text{partitions by quantile of } \{\hat{p}_j\}_{j=1}^N$</p> <p style="padding-left: 10px;">Find b such that $\hat{p}_i \in I_b$</p> <p style="padding-left: 10px;">$\text{Index}(I_b) \leftarrow \{j \hat{p}_j \in I_b\}$ ▷ get indices in bin b</p> <p style="padding-left: 10px;">$p_{\text{emp}}^i \leftarrow \frac{1}{ I_b } \sum_{i \in \text{Index}(I_b)} y_i$ ▷ empirical mean of bin b</p> <p>end function</p> <p>function KERNEL(r, K) ▷ r-window size; kernel</p> <p style="padding-left: 10px;">$N_r(i) \leftarrow r\text{-nearest neighbor of } \hat{p}_i \text{ (output probability space)}$</p> <p style="padding-left: 10px;">$Z \leftarrow \sum_{\hat{p}_j \in N_r(i)} K(\hat{p}_i, \hat{p}_j)$ ▷ normalization factor</p> <p style="padding-left: 10px;">$p_{\text{emp}}^i \leftarrow \sum_{\hat{p}_j \in N_r(i)} K(\hat{p}_i, \hat{p}_j) y_j / Z$ ▷ kernel smooth</p> <p>end function</p>
---	---

where p_{emp}^i is an estimate of the conditional probability $\mathbb{P}[y = 1 | f(\mathbf{x}) \in I(f(\mathbf{x}_i))]$ and $I(f(\mathbf{x}_i))$ is a small interval centered at $f(\mathbf{x}_i)$. As explained in Section 3 if $f(\mathbf{x}_i)$ is close to this value, then the model is well calibrated. We consider two approaches for estimating p_{emp}^i . (1) CaPE (bin) where we divide the training set into bins, select the bin b_i containing $f(\mathbf{x}_i)$ and set $p_{\text{emp}}^i = p_{\text{emp}}^{(b_i)}$ in equation 2. (2) CaPE (kernel) where p_{emp}^i is estimated through a moving average with a kernel function (see Appendix G for more details). Both methods are efficiently computed by sorting the predictions \hat{p}_i . The calibration loss requires a reasonable estimation of the empirical probabilities $p_{\text{emp}}^{(i)}$, which can be obtained from the model after early learning. Therefore using the calibration loss from the beginning is counterproductive, as demonstrated in Section L.

CaPE is summarized in Algorithm 1. Figures 4 and 5 show that incorporating the calibration-loss minimization step indeed preserves calibration as training proceeds (this is not necessarily expected because CaPE minimizes a calibration loss *on the training data*), and prevents the model from overfitting the observed outputs. This is beneficial also for the discriminative ability of the model, because it enables it to further reduce the cross-entropy loss without overfitting, as shown in Figure 5. The experiments with synthetic and real-world data reported in Section 7 suggest that this approach results in accurate probability estimates across a variety of realistic scenarios.

6 RELATED WORK

Neural networks trained for classification often generate a probability associated with their prediction which quantifies its uncertainty. These estimates have been found to be inaccurate in certain situations (Mukhoti et al., 2020; Guo et al., 2017). Techniques mitigating this issue are usually described as calibration methods, and broadly fall into three categories depending on whether they: (1)

Methods ($\times 10^{-2}$)	<i>Linear</i>		<i>Sigmoid</i>		<i>Centered</i>		<i>Skewed</i>		<i>Discrete</i>	
	MSE _p	KL _p	MSE _p	KL _p	MSE _p	KL _p	MSE _p	KL _p	MSE _p	KL _p
Infinite Data*	1.13	2.81	5.35	14.86	0.20	0.41	0.22	0.92	1.52	3.64
CE early-stop	4.21	10.93	6.16	17.16	0.48	0.98	0.40	1.79	2.24	5.26
Temperature	2.71	6.70	6.13	17.05	0.48	0.98	0.40	1.75	2.20	5.12
Platt Scaling	2.48	6.06	5.78	16.12	0.41	0.83	0.39	1.71	2.06	4.82
Dirichlet Cal.	3.56	9.06	8.71	25.33	0.46	0.94	0.48	2.31	2.74	6.52
Mix-n-match	2.69	6.70	6.13	17.10	0.48	0.98	0.39	1.74	2.20	5.12
Focal Loss	4.13	10.51	6.89	19.51	0.48	0.97	1.27	11.61	2.92	6.76
Entropy Reg.	2.84	7.37	7.03	21.19	0.42	0.87	1.17	10.57	2.84	6.62
MMCE Reg.	2.22	5.65	5.33	15.03	0.44	0.90	0.54	2.43	2.08	4.90
Deep Ensemble	1.90	4.55	5.85	16.43	0.44	0.89	0.55	2.58	1.97	4.61
CaPE (bin)	1.83	4.46	5.29	14.59	0.38	0.78	0.40	1.72	1.83	4.31
CaPE (kernel)	1.81	4.41	5.22	14.47	0.40	0.81	0.39	1.70	1.85	4.36

Table 1: Results on synthetic data. Appendix C.1 shows a table with confidence intervals obtained via bootstrapping. * is a model trained with infinite data obtained by continuous label resampling. The proposed method CaPE consistently outperforms existing techniques.

postprocess the outputs of a trained model, (2) combine multiple model outputs, or (3) modify the training process.

Post-processing methods transform the output probabilities in order to improve calibration on held-out data (Zadrozny & Elkan, 2001; Gupta et al., 2021; Kull et al., 2017; 2019). For example, Platt scaling (Platt, 1999) fits a logistic function that minimizes the negative log-likelihood loss. Temperature scaling (Guo et al., 2017) does the same with a temperature parameter augmenting the softmax function. In contrast to these methods, CaPE enforces calibration *during training*, which has the advantage of enabling further improvements in the discriminative abilities of the model.

Ensembling methods combine multiple models to improve generalization. Mix-n-Match (Zhang et al., 2020) uses a single model, and ensembles predictions using multiple temperature scaling transformations. Other methods (Lakshminarayanan et al., 2017; Maddox et al., 2019) ensemble multiple models obtained using different initializations. These approaches are compatible with the proposed method CaPE; how to combine them effectively is an interesting future research direction.

Modified training methods can be divided into two groups. The first group smooths the target 0/1 labels in order to prevent output estimates from collapsing to 0/1 (Mukhoti et al., 2020; Szegedy et al., 2016; Zhang et al., 2018; Thulasidasan et al., 2020). The second group, attaches additional calibration penalties to a cross entropy loss (Kumar et al., 2018; Pereyra et al., 2017; Liang et al., 2020). CaPE is most similar in spirit to the latter methods, although its data-driven calibration loss is different to the penalties used in these techniques.

Datasets for evaluation The methods discussed in this section were developed for calibration in classification, and tested on datasets such as CIFAR-10/100 (Krizhevsky, 2009), SVHN (Netzer et al., 2011), and ImageNet (Deng et al., 2009) where the relationship between labels and input data is *completely deterministic*. Here, we evaluate these methods on synthetic and real-world probability-estimation problems with inherent uncertainty.

7 EXPERIMENTS

7.1 SYNTHETIC DATASET: FACE-BASED RISK PREDICTION

To benchmark probability-estimation methods, we build a synthetic dataset based on UTK-Face (Zhang et al., 2017b), containing face images and associated ages. We use the age of the i th person z_i to assign them a risk of contracting a disease $p_i = \psi(z_i)$ for a fixed function $\psi : \mathbb{Z}_{\geq 0} \rightarrow [0, 1]$. Then we simulate whether the person actually contracts the illness (label $y_i = 1$) or not ($y_i = 0$) with probability p_i . The probability-estimation task is to estimate the ground-truth probability p_i from the face image x_i using a model that only has access to the images and the binary observations during training. This requires learning to discriminate age and map it to the corresponding risk. We design ψ to create five scenarios, inspired by real-world data (see Appendix I):

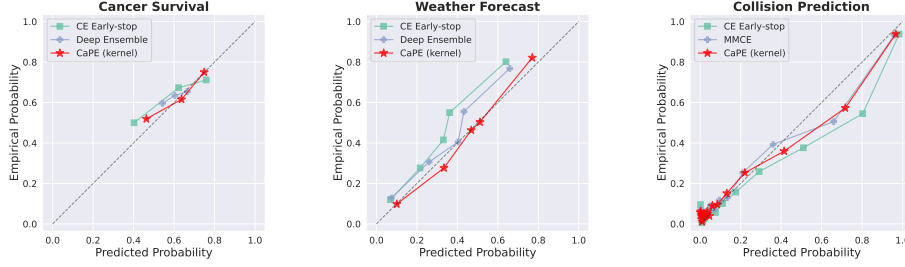


Figure 6: **Reliability diagrams for real-world data.** Reliability diagrams of binned mean predicted and empirical probabilities (see Section 3). The dashed line indicates perfect calibration. The results are computed on test data for cross-entropy minimization with early stopping, the proposed method (CaPE) and the best baseline for each dataset. CaPE produces better calibrated outputs. Appendix C.3 shows additional reliability diagrams.

- **Linear:** Equally-spaced, inspired by weather forecasting: $\psi(z) = z/100$
- **Sigmoid:** Concentrated near two extremes: $\psi(z) = \sigma(25(z/100 - 0.29))$
- **Skewed:** Clustered close to zero, inspired by vehicle-collision detection: $\psi(z) = z/250$
- **Centered:** Clustered in the center, inspired by cancer-survival prediction: $\psi(z) = z/300 + 0.35$
- **Discrete:** Discretized: $\psi(z) = 0.2[\mathbb{1}_{\{z>20\}} + \mathbb{1}_{\{z>40\}} + \mathbb{1}_{\{z>60\}} + \mathbb{1}_{\{z>80\}}] + 0.1$

7.2 REAL-WORLD DATASETS

We use three open-source, real-world datasets to benchmark probability-estimation approaches (see Appendix J for further details on the datasets and experiments).

Survival of Cancer Patients. Histopathology aims to identify tumor cells, cancer subtypes, and the stage and level of differentiation of cancer. Hematoxylin and Eosin (H&E)-stained slides are the most common type of histopathology data used for clinical decision making. In particular, they can be used for survival prediction (Wulczyn et al., 2020), which is critical in evaluating the prognosis of patients. Treatments assigned to patients after diagnosis are not personalized and their impact on cancer trajectory is complex, so the survival status of a patient is not deterministic. In this work, we use the H&E slides of non-small cell lung cancers from The Cancer Genome Atlas Program (TCGA)³ to estimate the the 5-year survival probability of cancer patients. The outcome distribution is similar to the *Centered* scenario in Section 7.1.

Weather Forecasting. The atmosphere is governed by nonlinear dynamics, hence weather forecast models possess inherent uncertainties (Richardson, 2007). Nowcasting, weather prediction in the near future, is of great operational significance, especially with increasing number of extreme inclement weather conditions (Agrawal et al., 2019; Ravuri et al., 2021). We use the German Weather service dataset⁴, which contains quality-controlled rainfall-depth composites from 17 operational Doppler radars. We use 30 minutes of precipitation data to predict if the mean precipitation over the area covered will increase or decrease one hour after the most recent measurement. Three precipitation maps from the past 30 minutes serve as an input. The outcome distribution is similar to the *Linear* scenario in Section 7.1.

Collision Prediction. Vehicle collision is one of the leading causes of death in the world. Reliable collision prediction systems are therefore instrumental in saving human lives. These systems predict potential collisions from dashcam cameras. Collisions are influenced by many unknown factors, and hence are not deterministic. Following Kim et al. (2019), we use 0.3 seconds of real dashcam videos from YouTubeCrash dataset as input, and predict the probability of a collision in the next 2 seconds. The data are very imbalanced as the number of collisions is very low, so the outcome distribution is similar to the *Skewed* scenario in Section 7.1.

³<https://www.cancer.gov/tcga>

⁴<https://opendata.dwd.de/weather/radar/>

Method ($\times 10^{-2}$)	Cancer Survival			Weather forecasting			Collision Prediction		
	AUC	ECE	Brier	AUC	ECE	Brier	AUC	ECE	Brier
CE early-stop	58.88	12.25	23.96	77.64	10.91	20.57	85.68	4.36	8.59
Temperature	58.88	12.07	23.73	77.64	8.66	20.21	85.68	4.56	8.51
Platt Scaling	58.91	10.28	23.33	77.65	6.97	19.53	85.76	3.04	8.23
Dirichlet Cal.	49.89	13.83	24.08	77.51	14.29	21.89	83.36	5.78	8.78
Mix-n-match	58.88	12.16	23.67	77.64	8.65	20.21	85.68	4.40	8.52
Focal Loss	55.02	12.15	23.31	76.18	8.32	20.27	82.21	9.07	9.82
Entropy Reg.	56.29	11.73	23.62	79.01	10.53	19.77	83.15	14.54	11.10
MMCE Reg.	48.45	11.84	23.73	76.69	8.46	20.12	85.18	2.94	8.48
Deep Ensemble	52.46	9.99	23.47	79.86	7.41	18.82	85.27	3.15	8.55
CaPE (bin)	61.44	12.31	23.20	78.99	5.16	18.37	85.70	3.16	8.18
CaPE (kernel)	61.22	9.48	23.18	79.00	5.08	18.39	85.95	3.22	8.13

Table 2: Results on cancer-survival prediction, weather forecasting, and collision prediction. Tables with all the metrics described in Section 3 are provided in Appendix C.2. The proposed method CaPE outperforms existing techniques in terms of Brier score, the metric that best captures probability-estimation accuracy.

7.3 BASELINES

We apply existing calibration methods developed for classification to probability estimation (as well as cross-entropy minimization with early-stopping): (1) **Three post-processing methods:** Temperature Scaling (Guo et al., 2017), Platt Scaling (Platt, 1999), and Dirichlet Calibration (Kull et al., 2019) applied to the best CE model, (2) **Two Ensemble Methods:** Mix-n-Match (Zhang et al., 2020) applied to best CE model, and Deep Ensemble (Lakshminarayanan et al., 2017) with 5 networks, and (3) **Three Modified Training methods:** focal loss (Mukhoti et al., 2020), entropy-maximizing loss (Pereyra et al., 2017), and MMCE regularization (Kumar et al., 2018). Appendix H provides a detailed description. For our experiments on synthetic data, we also compare against a model trained on an **infinite amount of data** by repeatedly sampling new outcomes from the ground-truth probabilities at each epoch. This provides a best-case reference for each scenario.

8 RESULTS AND DISCUSSION

Table 1 shows that calibration methods developed for classification can be effective for probability estimation. However, the performance of some methods is not consistent across all scenarios. For instance, regularization with negative entropy, which penalizes very high/low confidence, performs worse than CE when the ground-truth probability is close to 0 or 1. In contrast, methods that do not make strong assumptions tend to generalize better to multiple scenarios (e.g. Platt scaling consistently beats CE). The proposed method CaPE outperforms other techniques in most scenarios, and even matches the performance of the *infinite data* baseline for the *Sigmoid* scenario. Finally, we observe that the *Skewed* scenario is very challenging: most methods barely improve the CE baseline.

Table 2 compares the baseline methods and CaPE on the three real-world datasets. We present AUC, ECE for 15 equally-sized bins, and Brier score, as complementary metrics since the underlying ground-truth probabilities are unobserved. As discussed in Section 3, Brier score is the metric that best captures the quality of probability estimates. CaPE has the lowest Brier score in all three datasets, while also achieving lower ECE values and higher AUC values than most other methods. This demonstrates that enforcing calibration during training also yields a more discriminative model. The reliability diagrams in Figure 6 depict the probability estimates produced by CE, CaPE and the best baseline method on the three datasets, demonstrating that CaPE produces outputs that are better calibrated on real data.

Figure 6 also shows that each real-world dataset closely aligns with a particular synthetic scenario: cancer survival with *Centered*; weather forecasting with *Linear*; collision prediction with *Skewed*. This supports the significance of our synthetic benchmark dataset, and provides insights in the differences among baseline models. For example, model averaging with deep ensemble performs well on weather forecasting but has higher Brier scores than Platt scaling on the other two datasets (see Appendix K for further analysis based on pathological stages). Accordingly, deep ensemble also underperforms in the synthetic scenarios where ground-truth probabilities are clustered closely (*Sig-*

moid, *Linear*), but is effective for *Linear*. Finally, as in the synthetic *Skewed* scenario, all methods had similar performance on the collision prediction task. This highlights the importance of considering different scenarios when evaluating methodology for probability estimation.

9 CONCLUSION

In this work we evaluate existing approaches to improve the output probabilities of neural networks on probability-estimation problems. To this end, we introduce a new synthetic benchmark dataset designed to reproduce several realistic scenarios, and also gather three real-world datasets relevant to medicine, climatology, and self-driving cars. In addition, we provide theoretical analysis showing that early learning and memorization are fundamental phenomena in high-dimensional probability estimation. Motivated by this, we propose a novel approach that outperforms existing approaches on our simulated and real-world benchmarks. An important application for probability estimation is in the context of survival analysis, which can be recast as estimation of conditional probabilities (Lee et al., 2018; Shamout et al., 2020; Goldstein et al., 2021). Another interesting research direction is to consider problems with several possible uncertain outcomes (analogous to multiclass classification).

ACKNOWLEDGMENTS

The authors gratefully acknowledge support from Alzheimer’s Association grant AARG-NTF-21-848627 (S.L.), NIH grant R01 LM01331 (A.K., B.Y.), NSF grants HDR-1940097 (M.L.), DMS-2009752 (C.F.G., S.L.) and NRT-1922658 (A.K., S.L., S.M., B.Y., W.Z.), and the NYU Langone Health Predictive Analytics Unit (N.R., W.Z.). C.F.G. would like to thank Juan Argote for useful discussions.

REFERENCES

- Shreya Agrawal, Luke Barrington, Carla Bromberg, John Burge, Cenk Gazen, and Jason Hickey. Machine learning for precipitation nowcasting from radar images. *arXiv preprint arXiv:1912.12132*, 2019.
- Georgy Ayzel. Rainnet: a convolutional neural network for radar-based precipitation nowcasting. <https://github.com/hydrogo/rainnet>, 2020.
- Andreas Buja, Werner Stuetzle, and Yi Shen. Loss functions for binary class probability estimation and classification: Structure and applications,” manuscript, available at www-stat.wharton.upenn.edu/~buja, 2005.
- Xinlei Chen, Haoqi Fan, Ross B. Girshick, and Kaiming He. Improved baselines with momentum contrastive learning. *CoRR*, abs/2003.04297, 2020. URL <https://arxiv.org/abs/2003.04297>.
- Jia Deng, Wei Dong, Richard Socher, Li-Jia Li, Kai Li, and Li Fei-Fei. Imagenet: A large-scale hierarchical image database. In *2009 IEEE Conference on Computer Vision and Pattern Recognition*, pp. 248–255, 2009. doi: 10.1109/CVPR.2009.5206848.
- Yarin Gal and Zoubin Ghahramani. Dropout as a bayesian approximation: Representing model uncertainty in deep learning, 2016.
- Mark Goldstein, Xintian Han, Aahlad Puli, Adler J. Perotte, and Rajesh Ranganath. X-cal: Explicit calibration for survival analysis, 2021.
- Ian Goodfellow, Yoshua Bengio, Aaron Courville, and Yoshua Bengio. *Deep learning*, volume 1. MIT Press, 2016.
- Chuan Guo, Geoff Pleiss, Yu Sun, and Kilian Q Weinberger. On calibration of modern neural networks. In *International Conference on Machine Learning*, pp. 1321–1330. PMLR, 2017.
- Kartik Gupta, Amir Rahimi, Thalaiyasingam Ajanthan, Thomas Mensink, Cristian Sminchisescu, and Richard Hartley. Calibration of neural networks using splines. In *International Conference on Learning Representations*, 2021. URL <https://openreview.net/forum?id=eQe8DEWNN2W>.
- Maximilian Ilse, Jakub Tomczak, and Max Welling. Attention-based deep multiple instance learning. In Jennifer Dy and Andreas Krause (eds.), *Proceedings of the 35th International Conference on Machine Learning*, volume 80 of *Proceedings of Machine Learning Research*, pp. 2127–2136. PMLR, 10–15 Jul 2018. URL <https://proceedings.mlr.press/v80/ilse18a.html>.
- Hoon Kim, Kangwook Lee, Gyeongjo Hwang, and Changho Suh. Crash to not crash: Learn to identify dangerous vehicles using a simulator. In *Proceedings of the AAAI Conference on Artificial Intelligence*, volume 33, pp. 978–985, 2019.
- Alex Krizhevsky. Learning multiple layers of features from tiny images. Technical report, 2009.
- Meelis Kull, Telmo M. Silva Filho, and Peter Flach. Beyond sigmoids: How to obtain well-calibrated probabilities from binary classifiers with beta calibration. *Electronic Journal of Statistics*, 11(2):5052 – 5080, 2017. doi: 10.1214/17-EJS1338SI. URL <https://doi.org/10.1214/17-EJS1338SI>.
- Meelis Kull, Miquel Perelló-Nieto, Markus Kängsepp, Telmo de Menezes e Silva Filho, Hao Song, and Peter A. Flach. Beyond temperature scaling: Obtaining well-calibrated multiclass probabilities with dirichlet calibration. In *NeurIPS*, 2019.
- Aviral Kumar, Sunita Sarawagi, and Ujjwal Jain. Trainable calibration measures for neural networks from kernel mean embeddings. In *ICML*, 2018.
- Balaji Lakshminarayanan, Alexander Pritzel, and Charles Blundell. Simple and scalable predictive uncertainty estimation using deep ensembles, 2017.

- Changhee Lee, William Zame, Jinsung Yoon, and Mihaela van der Schaar. Deephit: A deep learning approach to survival analysis with competing risks. *Proceedings of the AAAI Conference on Artificial Intelligence*, 32(1), Apr. 2018. URL <https://ojs.aaai.org/index.php/AAAI/article/view/11842>.
- Gongbo Liang, Yu Zhang, Xiaoqin Wang, and Nathan Jacobs. Improved trainable calibration method for neural networks on medical imaging classification. In *British Machine Vision Conference (BMVC)*, 2020.
- Sheng Liu, Jonathan Niles-Weed, Narges Razavian, and Carlos Fernandez-Granda. Early-learning regularization prevents memorization of noisy labels. *Advances in Neural Information Processing Systems*, 33, 2020.
- Wesley Maddox, Timur Garipov, Pavel Izmailov, Dmitry P. Vetrov, and Andrew Gordon Wilson. A simple baseline for bayesian uncertainty in deep learning. *CoRR*, abs/1902.02476, 2019. URL <http://arxiv.org/abs/1902.02476>.
- Jishnu Mukhoti, Viveka Kulharia, Amartya Sanyal, S. Golodetz, Philip H. S. Torr, and P. Dokania. Calibrating deep neural networks using focal loss. *ArXiv*, abs/2002.09437, 2020.
- Yuval Netzer, Tao Wang, Adam Coates, Alessandro Bissacco, Bo Wu, and Andrew Y. Ng. Reading digits in natural images with unsupervised feature learning. 2011. URL http://ufldl.stanford.edu/housenumbers/nips2011_housenumbers.pdf.
- Gabriel Pereyra, George Tucker, Jan Chorowski, Lukasz Kaiser, and Geoffrey E. Hinton. Regularizing neural networks by penalizing confident output distributions. *CoRR*, abs/1701.06548, 2017. URL <http://arxiv.org/abs/1701.06548>.
- J. Platt. Probabilistic outputs for support vector machines and comparisons to regularized likelihood methods. *Advances in Large Margin Classifiers*, 10(3), 1999.
- Janis Postels, Francesco Ferroni, Huseyin Coskun, Nassir Navab, and Federico Tombari. Sampling-free epistemic uncertainty estimation using approximated variance propagation. *CoRR*, abs/1908.00598, 2019. URL <http://arxiv.org/abs/1908.00598>.
- Suman Ravuri, Karel Lenc, Matthew Willson, Dmitry Kangin, Remi Lam, Piotr Mirowski, Megan Fitzsimons, Maria Athanassiadou, Sheleem Kashem, Sam Madge, et al. Skillful precipitation nowcasting using deep generative models of radar. *arXiv preprint arXiv:2104.00954*, 2021.
- Lewis Fry Richardson. *Weather prediction by numerical process*. Cambridge university press, 2007.
- Farah E. Shamout, Yiqiu Shen, Nan Wu, Aakash Kaku, Jungkyu Park, Taro Makino, Stanislaw Jastrzebski, Duo Wang, Ben Zhang, Siddhant Dogra, Meng Cao, Narges Razavian, David Kudlowitz, Lea Azour, William Moore, Yvonne W. Lui, Yindalon Aphinyanaphongs, Carlos Fernandez-Granda, and Krzysztof J. Geras. An artificial intelligence system for predicting the deterioration of COVID-19 patients in the emergency department. *CoRR*, abs/2008.01774, 2020. URL <https://arxiv.org/abs/2008.01774>.
- Alexander Shekhovtsov and Boris Flach. Feed-forward propagation in probabilistic neural networks with categorical and max layers. In *International Conference on Learning Representations*, 2019. URL <https://openreview.net/forum?id=SkMuPjRcKQ>.
- Christian Szegedy, V. Vanhoucke, S. Ioffe, Jonathon Shlens, and Z. Wojna. Rethinking the inception architecture for computer vision. *2016 IEEE Conference on Computer Vision and Pattern Recognition (CVPR)*, pp. 2818–2826, 2016.
- Jeppe Thagaard, Søren Hauberg, Bert van der Vegt, Thomas Ebstrup, Johan D Hansen, and Anders B Dahl. Can you trust predictive uncertainty under real dataset shifts in digital pathology? In *International Conference on Medical Image Computing and Computer-Assisted Intervention*, pp. 824–833. Springer, 2020.
- Sunil Thulasidasan, Gopinath Chennupati, Jeff Bilmes, Tanmoy Bhattacharya, and Sarah Michalak. On mixup training: Improved calibration and predictive uncertainty for deep neural networks, 2020.

- Hao Wang, Xingjian Shi, and Dit-Yan Yeung. Natural-parameter networks: A class of probabilistic neural networks. *CoRR*, abs/1611.00448, 2016. URL <http://arxiv.org/abs/1611.00448>.
- Ellery Wulczyn, David F. Steiner, Zhaoyang Xu, Apaar Sadhwani, Hongwu Wang, I. Flament, C. Mermel, Po-Hsuan Cameron Chen, Yun Liu, and Martin C. Stumpe. Deep learning-based survival prediction for multiple cancer types using histopathology images. *PLoS ONE*, 15, 2020.
- Xiaobo Xia, Tongliang Liu, Bo Han, Chen Gong, Nannan Wang, Zongyuan Ge, and Yi Chang. Robust early-learning: Hindering the memorization of noisy labels. In *International Conference on Learning Representations*, 2020.
- Quanming Yao, Hansi Yang, Bo Han, Gang Niu, and James Tin-Yau Kwok. Searching to exploit memorization effect in learning with noisy labels. In *International Conference on Machine Learning*, pp. 10789–10798. PMLR, 2020.
- B. Zadrozny and C. Elkan. Obtaining calibrated probability estimates from decision trees and naive bayesian classifiers. In *ICML*, 2001.
- Chiyuan Zhang, Samy Bengio, Moritz Hardt, Benjamin Recht, and Oriol Vinyals. Understanding deep learning requires rethinking generalization. *ICLR*, 2017a.
- Hongyi Zhang, Moustapha Cissé, Yann Dauphin, and David Lopez-Paz. mixup: Beyond empirical risk minimization. *ArXiv*, abs/1710.09412, 2018.
- Jize Zhang, B. Kailkhura, and T. Y. Han. Mix-n-match: Ensemble and compositional methods for uncertainty calibration in deep learning. In *ICML*, 2020.
- Zhifei Zhang, Yang Song, and Hairong Qi. Age progression/regression by conditional adversarial autoencoder. In *IEEE Conference on Computer Vision and Pattern Recognition (CVPR)*. IEEE, 2017b.

A ANALYTICAL MODEL

In this appendix, we propose a simple analytical model that helps to demonstrate the early learning and memorization phenomena in probability estimation. Consider the following standard logistic regression problem: we are given i.i.d. data $\{(y_i, \mathbf{x}_i)\}_{i \leq n}$ where $y_i \in \{+1, -1\}$ are labels⁵ and $\mathbf{x}_i \sim \mathcal{N}(0, I_p)$ are standard Gaussian covariate vectors. Given $\mathbf{x}_i = \mathbf{x}$, the label y_i is distributed according to

$$\mathbb{P}(y_i = 1 | \mathbf{x}_i = \mathbf{x}) = \sigma(\langle \boldsymbol{\theta}_p^*, \mathbf{x} \rangle), \quad (6)$$

where $\sigma(x) = (1 + e^{-x})^{-1}$ is the sigmoid function and $\boldsymbol{\theta}_p^* \in \mathbb{R}^p$ is the ground-truth parameter with Euclidean norm $\|\boldsymbol{\theta}_p^*\| = \gamma > 0$. Throughout, we assume that we are working in the high dimensional regime: the ratio $\frac{p}{n} \rightarrow \kappa \in (0, +\infty)$ as $n \rightarrow \infty$. For convenience, we denote N_0 an integer such that $\frac{p}{n} < 2\kappa$ for $\forall n > N_0$. In Section B of the appendix, we provide a numerical example to illustrate this theoretical model.

Given a fresh sample $\mathbf{z} \in \mathbb{R}^p$, we predict the probability of the associated label being one via $\sigma(\langle \hat{\boldsymbol{\theta}}, \mathbf{z} \rangle)$ for some $\hat{\boldsymbol{\theta}} \in \mathbb{R}^p$, and we train the estimator $\hat{\boldsymbol{\theta}}$ through gradient descent to minimize the cross-entropy:

$$L_n(\boldsymbol{\theta}) = -\frac{1}{n} \sum_{i=1}^n \left\{ \left(\frac{1+y_i}{2} \right) \log \sigma(\langle \boldsymbol{\theta}, \mathbf{x}_i \rangle) + \left(\frac{1-y_i}{2} \right) \log(1 - \sigma(\langle \boldsymbol{\theta}, \mathbf{x}_i \rangle)) \right\} \quad (7)$$

$$= \frac{1}{n} \sum_{i=1}^n \left\{ -\frac{1}{2} y_i \langle \boldsymbol{\theta}, \mathbf{x}_i \rangle + \log \left(e^{\frac{1}{2} \langle \boldsymbol{\theta}, \mathbf{x}_i \rangle} + e^{-\frac{1}{2} \langle \boldsymbol{\theta}, \mathbf{x}_i \rangle} \right) \right\} \quad (8)$$

$$\hat{\boldsymbol{\theta}}_{\eta,n}^{k+1} = \hat{\boldsymbol{\theta}}_{\eta,n}^k - \eta \nabla L_n(\hat{\boldsymbol{\theta}}_{\eta,n}^k), \quad k = 0, 1, \dots \quad (9)$$

where we choose constant step size $\eta < \delta$, for some prefixed $\delta > 0$, to be determined later. For the initialization, we draw $\hat{\boldsymbol{\theta}}_{\eta,n}^0$ uniformly from the sphere of radius γ_0 .

Define the mean squared error

$$\text{MSE}_{\eta,n}(k) := \mathbb{E}[(\sigma(\langle \hat{\boldsymbol{\theta}}_{\eta,n}^k, \mathbf{z} \rangle) - \sigma(\langle \boldsymbol{\theta}_p^*, \mathbf{z} \rangle))^2], \quad (10)$$

where $\mathbf{z} \sim \mathcal{N}(0, I_p)$ is a fresh Gaussian vector, independent of the data. Note that the expectation is taken with respect to all sources of randomness (including the randomness of data and initialization).

We present two main theorems that summarize our results. The first theorem states that for sufficiently large n and p , the mean squared error decreases during the initial iterates of gradient descent. This phenomenon justifies the name ‘‘early learning’’: during early stages of training, the predictions obtained by the iterates of gradient descent improve.

Theorem A.1. *For any $n > N^*$, the function $k \mapsto \text{MSE}_{\eta,n}(k)$ decreases for $k \in [0, \frac{T^*}{\eta})$, where the constants $N^* = N^*(\eta, \gamma, \gamma_0)$ depends on η, γ, γ_0 and $T^* = T^*(\kappa, \gamma, \gamma_0, \delta) > 0$ depends on κ, γ, γ_0 , and δ .*

The second theorem, however, states that when the dimension is sufficiently large (with respect to the number of samples), the predictor eventually overfits, and converges to a predictor that outputs only the probabilities 0 and 1.

Theorem A.2. *Let $p(\mathbf{z}) = \lim_{k \rightarrow \infty} \sigma(\langle \hat{\boldsymbol{\theta}}_{\eta,n}^k, \mathbf{z} \rangle)$. Then there exists a $\kappa^* = \kappa^*(\gamma)$, such that when $n \rightarrow +\infty$ and $\frac{p}{n} \rightarrow \kappa > \kappa^*$, we have*

$$\mathbb{P}(\{p(\mathbf{z}) \in \{0, 1\} \text{ for a.e. } \mathbf{z} \in \mathbb{R}^p\}) \rightarrow 1.$$

We begin with the proof of Theorem A.2.

Proof of Theorem A.2. Define the event

$$S_n = \{\exists \mathbf{w} \in \mathbb{R}^p \text{ such that for } \forall i \leq n : y_i \langle \mathbf{w}, \mathbf{x}_i \rangle > 0\}.$$

⁵For mathematical convenience, in this appendix we work with labels in $\{\pm 1\}$ rather than $\{0, 1\}$.

For some large $C_G > 0$ to be determined later, define the event

$$G_n = \{\|X\|_2 \leq C_G(\sqrt{n} + \sqrt{p})\},$$

where $X = (\mathbf{x}_1, \dots, \mathbf{x}_n) \in \mathbb{R}^{p \times n}$ is the covariate matrix and $\|X\|_2$ denotes the maximum singular value of X . Pick $\delta < \frac{2}{C_G^2(\sqrt{\kappa}+1)^2}$.

We claim that $S_n \cap G_n \subset E_n = \{p(\mathbf{z}) \in \{0, 1\} \text{ for a.e. } \mathbf{z} \in \mathbb{R}^p\}$. Indeed, assume that S_n and G_n happen. Then the step size η satisfies

$$\eta < \delta < \frac{2}{C_G^2(\sqrt{\kappa}+1)^2} < \frac{2n}{\|X\|_2^2}.$$

On the event S_n , the data points are separable, and ? , Theorem 3 implies that as $k \rightarrow \infty$,

$$\begin{aligned} \|\hat{\boldsymbol{\theta}}_{\eta,n}^k\|_2 &\rightarrow +\infty, \\ \frac{\hat{\boldsymbol{\theta}}_{\eta,n}^k}{\|\hat{\boldsymbol{\theta}}_{\eta,n}^k\|_2} &\rightarrow \hat{\boldsymbol{\theta}}^{MM}, \end{aligned}$$

where $\hat{\boldsymbol{\theta}}^{MM} \in \mathbb{R}^p$ denotes the max-margin separator. Thus for any $\mathbf{z} \in \mathbb{R}^p$ with $\langle \mathbf{z}, \hat{\boldsymbol{\theta}}^{MM} \rangle > 0$ (resp. < 0), we have $\langle \mathbf{z}, \hat{\boldsymbol{\theta}}_{\eta,n}^k \rangle \rightarrow +\infty$ (resp. $-\infty$), and thus $p(\mathbf{z}) = \lim_{k \rightarrow \infty} \sigma(\langle \hat{\boldsymbol{\theta}}_{\eta,n}^k, \mathbf{z} \rangle) = 1$ (resp. $= 0$). Since $\{\mathbf{z} \in \mathbb{R}^p : \langle \mathbf{z}, \hat{\boldsymbol{\theta}}^{MM} \rangle = 0\}$ has Lebesgue measure 0, we have shown that $S_n \cap G_n \subset E_n$.

It remains to show that S_n and G_n hold with probability tending to one. ? , Theorem 1 show that there exists a finite threshold κ^* , such that when $\frac{p}{n} \rightarrow \kappa > \kappa^*$, it holds that $\mathbb{P}(S_n) \rightarrow 1$. Moreover, by standard results from random matrix theory [see e.g. ? , Theorem 4.4.5], there exists some constant C_G such that $\mathbb{P}(G_n) \geq 1 - 2e^{-n} \rightarrow 1$. Therefore, we can conclude that

$$\mathbb{P}(E_n) \geq \mathbb{P}(S_n \cap G_n) \rightarrow 1.$$

□

In the remainder of the appendix, we prove Theorem A.1. Consider the following gradient flow, which is the analogue of gradient descent in the $\eta \rightarrow 0$ limit.

$$\frac{d\hat{\boldsymbol{\theta}}_n^t}{dt} = -\nabla L_n(\hat{\boldsymbol{\theta}}_n^t), \quad \forall t \geq 0. \quad (11)$$

Set $\hat{\boldsymbol{\theta}}_n^0 = \hat{\boldsymbol{\theta}}_{\eta,n}^0$ and define the corresponding mean square error

$$\text{MSE}_n(t) := \mathbb{E}[(\sigma(\langle \hat{\boldsymbol{\theta}}_n^t, \mathbf{z} \rangle) - \sigma(\langle \boldsymbol{\theta}_p^*, \mathbf{z} \rangle))^2]. \quad (12)$$

We will first show that the mean squared error decreases along the trajectory of gradient flow, and then establish that this result extends to the iterates of gradient descent. We denote $\text{MSE}_n'(t)$ as the derivative of MSE_n at time $t \geq 0$.

Lemma A.3. (a) $\lim_{n \rightarrow \infty} \text{MSE}_n'(0) < 0$.

(b) There exists some positive constants $N_1(\gamma, \gamma_0)$, $T_1(\gamma, \gamma_0)$ and $C_1(\gamma, \gamma_0)$, such that for any $n > N_1$ and $t < T_1$, it holds that

$$\text{MSE}_n'(t) \leq -C_1.$$

Proof. (a) For convenience, we write equation (11) in matrix form

$$\frac{d\hat{\boldsymbol{\theta}}_n^t}{dt} = \frac{1}{n} X(\mathbf{y}' - \sigma(X^T \hat{\boldsymbol{\theta}}_n^t)),$$

where $X = (\mathbf{x}_1, \dots, \mathbf{x}_n) \in \mathbb{R}^{p \times n}$, $\mathbf{y}' = (\frac{y_1+1}{2}, \dots, \frac{y_n+1}{2})^T \in \mathbb{R}^n$ and $\sigma(X^T \hat{\boldsymbol{\theta}}_n^t) = (\sigma(\langle \mathbf{x}_1, \hat{\boldsymbol{\theta}}_n^t \rangle), \dots, \sigma(\langle \mathbf{x}_n, \hat{\boldsymbol{\theta}}_n^t \rangle))^T \in \mathbb{R}^n$. We first calculate the derivative of the mean square pre-

diction error:

$$\begin{aligned} \text{MSE}'_n(t) &= \mathbb{E} \left[\left(\sigma(\langle \hat{\theta}_n^t, z \rangle) - \sigma(\langle \theta_p^*, z \rangle) \right) \sigma'(\langle \hat{\theta}_n^t, z \rangle) \left\langle \frac{d\hat{\theta}_n^t}{dt}, z \right\rangle \right] \\ &= \mathbb{E} \left[\left(\sigma(\langle \hat{\theta}_n^t, z \rangle) - \sigma(\langle \theta_p^*, z \rangle) \right) \sigma'(\langle \hat{\theta}_n^t, z \rangle) \frac{1}{n} (\mathbf{y}' - \sigma(X^T \hat{\theta}_n^t))^T X^T z \right] \\ &= \mathbb{E} \left[\left(\sigma(\langle \hat{\theta}_n^t, z \rangle) - \sigma(\langle \theta_p^*, z \rangle) \right) \sigma'(\langle \hat{\theta}_n^t, z \rangle) \frac{1}{n} (\sigma(X^T \theta_p^*) - \sigma(X^T \hat{\theta}_n^t))^T X^T z \right], \end{aligned}$$

where in the first line we used dominated convergence theorem, and in the last line we used $\mathbb{E}[\mathbf{y}'|X] = \sigma(X^T \theta_p^*)$.

Thus,

$$\begin{aligned} \text{MSE}'_n(0) &= \frac{1}{n} \sum_{i=1}^n \mathbb{E} \left[\left(\sigma(\langle \hat{\theta}_n^0, z \rangle) - \sigma(\langle \theta_p^*, z \rangle) \right) \sigma'(\langle \hat{\theta}_n^0, z \rangle) \left(\sigma(\langle \theta_p^*, x_i \rangle) - \sigma(\langle \hat{\theta}_n^0, x_i \rangle) \right) \langle x_i, z \rangle \right] \\ &= \mathbb{E} \left[\left(\sigma(\langle \hat{\theta}_n^0, z \rangle) - \sigma(\langle \theta_p^*, z \rangle) \right) \sigma'(\langle \hat{\theta}_n^0, z \rangle) \left(\sigma(\langle \theta_p^*, x_1 \rangle) - \sigma(\langle \hat{\theta}_n^0, x_1 \rangle) \right) \langle x_1, z \rangle \right], \end{aligned}$$

where $\hat{\theta}_n^0$, z , and x_1 are mutually independent. Let $\mu(b) := \mathbb{E}[\sigma'(Z_b)]$, where the scalar $Z_b \sim \mathcal{N}(0, b^2)$. Conditioned on $(z, \hat{\theta}_n^0)$, the pair $(\langle x_1, z \rangle, \langle \hat{\theta}_n^0, x_1 \rangle)$ is multivariate Gaussian with covariance $\langle \hat{\theta}_n^0, z \rangle$. By the Gaussian integration by parts formula,

$$\mathbb{E}[\sigma(\langle \hat{\theta}_n^0, x_1 \rangle) \langle x_1, z \rangle | z, \hat{\theta}_n^0] = \mathbb{E}[\sigma'(\langle \hat{\theta}_n^0, x_1 \rangle) | z, \hat{\theta}_n^0] \langle \hat{\theta}_n^0, z \rangle = \mu(\gamma_0) \langle \hat{\theta}_n^0, z \rangle.$$

Similarly,

$$\mathbb{E}[\sigma(\langle \theta_p^*, x_1 \rangle) \langle x_1, z \rangle | z, \theta_p^*] = \mu(\gamma) \langle \theta_p^*, z \rangle.$$

So

$$\text{MSE}'_n(0) = \mathbb{E} \left[\left(\sigma(\langle \hat{\theta}_n^0, z \rangle) - \sigma(\langle \theta_p^*, z \rangle) \right) \sigma'(\langle \hat{\theta}_n^0, z \rangle) \left(\mu(\gamma) \langle \theta_p^*, z \rangle - \mu(\gamma_0) \langle \hat{\theta}_n^0, z \rangle \right) \right],$$

Since $\hat{\theta}_n^0 \sim \text{Unif}(\mathbb{S}^{p-1}(\gamma_0))$, we have $\langle \hat{\theta}_n^0, \theta_p^* \rangle \rightarrow 0$ in probability as $p \rightarrow \infty$. Thus, the pair $(\langle \hat{\theta}_n^0, z \rangle, \langle \theta_p^*, z \rangle) \xrightarrow{d} (Z_0, Z)$, where Z_0 and Z are independent centered Gaussian random variables with variance γ_0 and γ , respectively.

We hence compute

$$\begin{aligned} \lim_{p \rightarrow \infty} \text{MSE}'_n(0) &= \mathbb{E}[(\sigma(Z_0) - \sigma(Z)) \sigma'(Z_0) (\mu(\gamma) Z - \mu(\gamma_0) Z_0)] \\ &= -\gamma^2 \mu(\gamma)^2 \mu(\gamma_0) - \mu(\gamma_0) \mathbb{E}[(\sigma(Z_0) - \frac{1}{2}) \sigma'(Z_0) Z_0], \end{aligned}$$

where in the last inequality we used Gaussian integration by parts and $\mathbb{E}[\sigma(Z)] = \frac{1}{2}$. Since $\mu(b) > 0$ for all $b \geq 0$ and $(\sigma(x) - \frac{1}{2}) \sigma'(x) x \geq 0$ for all $x \in \mathbb{R}$, we conclude that $\lim_{n \rightarrow \infty} \text{MSE}'_n(0) < 0$.

(b) We first show that the second derivative of MSE_n is uniformly bounded. Write $f(x) = (\sigma(x) - \sigma(\langle \theta_p^*, z \rangle))^2$. Since σ, σ' and σ'' are all bounded, we have

$$\begin{aligned} |\text{MSE}''_n(t)| &= \left| \mathbb{E} \left[f''(\langle \hat{\theta}_n^t, z \rangle) \left\langle \frac{d\hat{\theta}_n^t}{dt}, z \right\rangle^2 \right] + \mathbb{E} \left[f'(\langle \hat{\theta}_n^t, z \rangle) \left\langle \frac{d^2 \hat{\theta}_n^t}{dt^2}, z \right\rangle \right] \right| \\ &\leq C_1 \left(\mathbb{E} \left[\left\langle \frac{d\hat{\theta}_n^t}{dt}, z \right\rangle^2 \right] + \mathbb{E} \left[\left\| \left\langle \frac{d^2 \hat{\theta}_n^t}{dt^2}, z \right\rangle \right\| \right] \right) \\ &\leq C_2 \left(\mathbb{E} \left[\left\| \frac{d\hat{\theta}_n^t}{dt} \right\|_2^2 \right] + \mathbb{E} \left[\left\| \frac{d^2 \hat{\theta}_n^t}{dt^2} \right\|_2 \right] \right), \end{aligned}$$

where in the first equality, we use dominated convergence to interchange differentiation and expectation, and in the second inequality we used the fact that $z \sim \mathcal{N}(0, I_p)$ is independent of the data.

By a simple calculation,

$$\begin{aligned}\left\|\frac{d\hat{\theta}_n^t}{dt}\right\|_2 &\leq \frac{1}{n}\|X\|_2\left\|\mathbf{y}' - \sigma(X^T\hat{\theta}_n^t)\right\|_2 \leq \frac{2\sqrt{p}\|X\|_2}{n}, \\ \left\|\frac{d^2\hat{\theta}_n^t}{dt^2}\right\|_2 &= \left\|\frac{1}{n^2}XD_tX^TX(\mathbf{y}' - \sigma(X^T\hat{\theta}_n^t))\right\|_2 \leq \frac{2\sqrt{p}\|X\|_2^3}{n^2},\end{aligned}$$

where $D_t = \text{Diag}(\sigma'(\langle\hat{\theta}_n^t, \mathbf{x}_i\rangle))_{i=1}^n$ is a diagonal matrix with $\|D_t\|_2 \leq 1$. By standard random matrix results [see e.g. ?, Theorem 4.4.5],

$$\mathbb{E}[\|X\|_2^2] \leq C(\sqrt{p} + \sqrt{n})^2, \quad \mathbb{E}[\|X\|_2^3] \leq C(\sqrt{p} + \sqrt{n})^3.$$

Whence, for any $t \geq 0$ and $n > N_0$,

$$|\text{MSE}_n''(t)| \leq C_3 \left(\frac{p(\sqrt{p} + \sqrt{n})^2}{n^2} + \frac{\sqrt{p}(\sqrt{p} + \sqrt{n})^3}{n^2} \right) := L,$$

where $L = C_4(k^2 + 1)$ is a constant that only depends on κ .

Let $\tau = \tau(\gamma, \gamma_0) = \lim_{n \rightarrow \infty} \text{MSE}_n'(0)$, and let $N_1 = N_1(\gamma, \gamma_0) > N_0$ satisfy $\text{MSE}_n'(0) \leq \frac{\tau}{2}$ for any $n > N_1$. By Claim (a), $\tau < 0$. Then for any $t \leq T_1(\gamma, \gamma_0) = \frac{-\tau(\gamma, \gamma_0)}{4L}$,

$$\text{MSE}_n'(t) = \text{MSE}_n'(0) + (\text{MSE}_n'(t) - \text{MSE}_n'(0)) \leq \frac{\tau}{2} + Lt \leq \frac{\tau}{4}.$$

□

Lemma A.1 essentially shows that within a small constant time window, MSE_n' is negative, and thus the mean square error of gradient flow decreases. The next lemma shows that the mean square error of gradient flow is a good approximation of the mean square error of gradient descent. Before stating the next lemma, we extend gradient descent (9) to a piecewise linear function, i.e.

$$\frac{d\tilde{\theta}_{\eta,n}^t}{dt} = -\nabla L_n(\tilde{\theta}_{\eta,n}^{\lfloor t \rfloor}), \quad \forall t \geq 0, \quad (13)$$

where $\lfloor t \rfloor := \max\{k\eta : k\eta \leq t, k \in \mathbb{N}\}$. In particular, $\tilde{\theta}_{\eta,n}^{k\eta} = \hat{\theta}_{\eta,n}^k$.

Lemma A.4. (a) For any $t > 0$ and $n > N_0$,

$$\sup_{s \leq t} \|\tilde{\theta}_{\eta,n}^s - \hat{\theta}_n^s\| \leq C_2(\kappa, t, \delta, \gamma_0)\eta t.$$

with probability $1 - 2e^{-n}$, where $C_2(\kappa, t, \delta, \gamma_0) > 0$ is a constant that depends on κ, t, δ and γ_0 .

(b) For any $t > 0$ and $n > N_0$,

$$\sup_{k \leq t/\eta} |\text{MSE}_n(k\eta) - \text{MSE}_{\eta,n}(k)| \leq 4C_2(\kappa, t, \delta, \gamma_0)\eta t + 8e^{-n}.$$

Proof. (a) We first bound $\sup_{s \leq t} \|\tilde{\theta}_{\eta,n}^s - \hat{\theta}_n^s\|$.

Compute

$$\begin{aligned}\frac{d}{dt} \|\hat{\theta}_n^t\|_2 &\leq \left\|\frac{d\hat{\theta}_n^t}{dt}\right\|_2 \\ &= \left\|\frac{1}{n}X(\mathbf{y}' - \sigma(\mathbf{0})) + \frac{1}{n}X(\sigma(\mathbf{0}) - \sigma(X^T\hat{\theta}_n^t))\right\|_2 \\ &\leq \frac{2\sqrt{p}\|X\|_2}{n} + \frac{\|X\|_2^2\|\hat{\theta}_n^t\|_2}{n},\end{aligned}$$

where we used $\|\sigma(\mathbf{x}) - \sigma(\mathbf{y})\|_2 \leq \|\mathbf{x} - \mathbf{y}\|_2$ for any $\mathbf{x}, \mathbf{y} \in \mathbb{R}^p$. By Grönwall's inequality,

$$\|\hat{\theta}_n^t\|_2 \leq e^{\frac{\|X\|_2^2}{n}t} \left(\|\hat{\theta}_n^0\|_2 + \frac{2\sqrt{p}\|X\|_2}{n}t \right). \quad (14)$$

Next, compute

$$\begin{aligned}
\frac{d}{dt} \left\| \tilde{\boldsymbol{\theta}}_{\eta,n}^s - \hat{\boldsymbol{\theta}}_n^s \right\|_2 &\leq \left\| \frac{d}{dt} \left(\tilde{\boldsymbol{\theta}}_{\eta,n}^s - \hat{\boldsymbol{\theta}}_n^s \right) \right\|_2 \\
&= \left\| \frac{1}{n} X (\sigma(X^T \tilde{\boldsymbol{\theta}}_{\eta,n}^{\lfloor s \rfloor}) - \sigma(X^T \hat{\boldsymbol{\theta}}_n^s)) \right\|_2 \\
&\leq \frac{\|X\|_2^2}{n} \left\| \tilde{\boldsymbol{\theta}}_{\eta,n}^{\lfloor s \rfloor} - \hat{\boldsymbol{\theta}}_n^s \right\|_2 \\
&\leq \frac{\|X\|_2^2}{n} \left\| \tilde{\boldsymbol{\theta}}_{\eta,n}^s - \hat{\boldsymbol{\theta}}_n^s \right\|_2 + \frac{\|X\|_2^2}{n} \left\| \tilde{\boldsymbol{\theta}}_{\eta,n}^{\lfloor s \rfloor} - \tilde{\boldsymbol{\theta}}_{\eta,n}^s \right\|_2 \\
&\leq \frac{\|X\|_2^2}{n} \left\| \tilde{\boldsymbol{\theta}}_{\eta,n}^s - \hat{\boldsymbol{\theta}}_n^s \right\|_2 + \frac{\|X\|_2^2}{n} \left\| \tilde{\boldsymbol{\theta}}_{\eta,n}^{\lfloor s \rfloor} - \tilde{\boldsymbol{\theta}}_{\eta,n}^s \right\|_2.
\end{aligned}$$

Since $\tilde{\boldsymbol{\theta}}_{\eta,n}^s - \tilde{\boldsymbol{\theta}}_{\eta,n}^{\lfloor s \rfloor} = (s - \lfloor s \rfloor) \frac{1}{n} X (\mathbf{y}' - \sigma(X^T \tilde{\boldsymbol{\theta}}_{\eta,n}^{\lfloor s \rfloor}))$, we can bound

$$\begin{aligned}
\left\| \tilde{\boldsymbol{\theta}}_{\eta,n}^s - \tilde{\boldsymbol{\theta}}_{\eta,n}^{\lfloor s \rfloor} \right\|_2 &\leq \frac{2\eta\sqrt{p}\|X\|_2}{n} + \frac{\eta\|X\|_2^2\|\tilde{\boldsymbol{\theta}}_{\eta,n}^{\lfloor s \rfloor}\|_2}{n} \\
&\leq \frac{2\eta\sqrt{p}\|X\|_2}{n} + \frac{\eta\|X\|_2^2\|\hat{\boldsymbol{\theta}}_n^{\lfloor s \rfloor}\|_2}{n} + \frac{\eta\|X\|_2^2}{n} \left\| \hat{\boldsymbol{\theta}}_n^{\lfloor s \rfloor} - \tilde{\boldsymbol{\theta}}_{\eta,n}^{\lfloor s \rfloor} \right\|_2.
\end{aligned}$$

Combining the above inequalities, we get

$$\begin{aligned}
\frac{d}{dt} \sup_{s \leq t} \left\| \tilde{\boldsymbol{\theta}}_{\eta,n}^s - \hat{\boldsymbol{\theta}}_n^s \right\|_2 &\leq \frac{d}{dt} \left\| \tilde{\boldsymbol{\theta}}_{\eta,n}^t - \hat{\boldsymbol{\theta}}_n^t \right\|_2 \\
&\leq \frac{\|X\|_2^2}{n} \left\| \tilde{\boldsymbol{\theta}}_{\eta,n}^t - \hat{\boldsymbol{\theta}}_n^t \right\|_2 + \frac{\|X\|_2^2}{n} \left(\frac{2\eta\sqrt{p}\|X\|_2}{n} + \frac{\eta\|X\|_2^2\|\hat{\boldsymbol{\theta}}_n^{\lfloor t \rfloor}\|_2}{n} + \frac{\eta\|X\|_2^2}{n} \left\| \hat{\boldsymbol{\theta}}_n^{\lfloor t \rfloor} - \tilde{\boldsymbol{\theta}}_{\eta,n}^{\lfloor t \rfloor} \right\|_2 \right) \\
&\leq \left(\frac{\|X\|_2^2}{n} + \frac{\delta\|X\|_2^4}{n^2} \right) \sup_{s \leq t} \left\| \tilde{\boldsymbol{\theta}}_{\eta,n}^s - \hat{\boldsymbol{\theta}}_n^s \right\|_2 + \eta \left(\frac{2\sqrt{p}\|X\|_2^3}{n^2} + \frac{\|X\|_2^4\|\hat{\boldsymbol{\theta}}_n^{\lfloor t \rfloor}\|_2}{n^2} \right).
\end{aligned}$$

Together with inequality (14), by Grönwall's inequality we eventually have

$$\sup_{s \leq t} \left\| \tilde{\boldsymbol{\theta}}_{\eta,n}^s - \hat{\boldsymbol{\theta}}_n^s \right\|_2 \leq \eta t \left(\frac{2\sqrt{p}\|X\|_2^3}{n^2} + \frac{\gamma_0\|X\|_2^4 e^{\frac{\|X\|_2^2}{n}t}}{n^2} + \frac{2t\sqrt{p}\|X\|_2^5 e^{\frac{\|X\|_2^2}{n}t}}{n^3} \right) e^{(\frac{\|X\|_2^2}{n} + \frac{\delta\|X\|_2^4}{n^2})t}. \quad (15)$$

Again, by a standard random matrix result [see e.g. ?, Theorem 4.4.5], it holds that $\|X\|_2 \leq C(\sqrt{p} + \sqrt{n})$, with probability $1 - 2e^{-n}$. Plug this bound into inequality (15), we get for any $n > N_0$,

$$\sup_{s \leq t} \left\| \tilde{\boldsymbol{\theta}}_{\eta,n}^s - \hat{\boldsymbol{\theta}}_n^s \right\|_2 \leq \eta t C_2(\kappa, t, \delta, \gamma_0), \quad (16)$$

with probability $1 - 2e^{-n}$, where $C_2(\kappa, t, \delta, \gamma_0) = C(t + \gamma_0 + 1)(\kappa^6 + 1)e^{C(\delta+1)(\kappa^2+1)t}$, for some $C > 0$.

(b) Define the event $A_n = \left\{ \sup_{s \leq t} \left\| \tilde{\theta}_{\eta,n}^s - \hat{\theta}_n^s \right\|_2 \leq \eta t C_2(\kappa, t, \delta, \gamma_0) \right\}$. Since $|\sigma|, |\sigma'| < 1$, we have for any $n > N_0$,

$$\begin{aligned}
\sup_{k \leq t/\eta} |\text{MSE}_n(k\eta) - \text{MSE}_{\eta,n}(k)| &\leq \sup_{k \leq t/\eta} 4\mathbb{E}[\left| \sigma(\langle \hat{\theta}_n^{k\eta}, \mathbf{z} \rangle) - \sigma(\langle \hat{\theta}_{\eta,n}^k, \mathbf{z} \rangle) \right|] \\
&= \sup_{k \leq t/\eta} 4\mathbb{E}[\left| \sigma(\langle \hat{\theta}_n^{k\eta}, \mathbf{z} \rangle) - \sigma(\langle \hat{\theta}_{\eta,n}^k, \mathbf{z} \rangle) \right| \mathbb{1}_{A_n}] + 8e^{-n} \\
&\leq \sup_{k \leq t/\eta} 4\mathbb{E} \left[\left\| \hat{\theta}_n^{k\eta} - \hat{\theta}_{\eta,n}^k \right\|_2 \mathbb{1}_{A_n} \right] + 8e^{-n} \\
&\leq 4\mathbb{E} \left[\sup_{k \leq t/\eta} \left\| \hat{\theta}_n^{k\eta} - \hat{\theta}_{\eta,n}^k \right\|_2 \mathbb{1}_{A_n} \right] + 8e^{-n} \\
&= 4\mathbb{E} \left[\sup_{k \leq t/\eta} \left\| \hat{\theta}_n^{k\eta} - \tilde{\theta}_{\eta,n}^{k\eta} \right\|_2 \mathbb{1}_{A_n} \right] + 8e^{-n} \\
&\leq 4C_2(\kappa, t, \delta, \gamma_0)t\eta + 8e^{-n}
\end{aligned}$$

□

We are now ready to prove Theorem A.1.

Proof of Theorem A.1. Pick a small $T_2(\kappa, \delta, \gamma_0) > 0$ that satisfy $C_2(\kappa, T_2, \delta, \gamma_0)T_2 \leq \frac{C_1(\gamma, \gamma_0)}{32}$. This is possible since $C_2(\kappa, t, \delta, \gamma_0)$ is bounded as $t \rightarrow 0$. Let N_1 and T_1 be as in Lemma A.3, and let $T^*(\gamma, \gamma_0, \kappa, \delta) = \min\{T_1(\gamma, \gamma_0), T_2(\kappa, \delta, \gamma_0)\}$. For any $k < \frac{T^*}{\eta} - 1$,

$$\begin{aligned}
\text{MSE}_{\eta,n}(k+1) - \text{MSE}_{\eta,n}(k) &= (\text{MSE}_n((k+1)\eta) - \text{MSE}_n(k\eta)) + (\text{MSE}_{\eta,n}(k+1) - \text{MSE}_n((k+1)\eta)) \\
&\quad + (\text{MSE}_{\eta,n}(k) - \text{MSE}_n(k\eta)) \\
&\leq (\text{MSE}_n((k+1)\eta) - \text{MSE}_n(k\eta)) + 2 \sup_{m \leq T^*/\eta} |\text{MSE}_n(m\eta) - \text{MSE}_{\eta,n}(m)|
\end{aligned}$$

By Lemma A.3.(b) and the mean value theorem, for any $n > N_1$,

$$\text{MSE}_n((k+1)\eta) - \text{MSE}_n(k\eta) \leq -C_1(\gamma, \gamma_0)\eta.$$

By Lemma A.4.(b), it holds that for any $n > N_0$,

$$\begin{aligned}
\sup_{m \leq T^*/\eta} |\text{MSE}_n(m\eta) - \text{MSE}_{\eta,n}(m)| &\leq 4C_2(\kappa, T^*, \delta, \gamma_0)T^*\eta + 8e^{-n} \\
&\leq \frac{C_1(\gamma, \gamma_0)\eta}{8} + 8e^{-n}.
\end{aligned}$$

Let $N_2(\eta, \gamma, \gamma_0)$ satisfy $8e^{-N_2} < \frac{C_1(\gamma, \gamma_0)\eta}{8}$, and let $N^*(\eta, \gamma, \gamma_0) = \max\{N_1(\gamma, \gamma_0), N_2(\eta, \gamma, \gamma_0)\}$. We therefore have for any $n > N^*$ and $k < \frac{T^*}{\eta} - 1$,

$$\begin{aligned}
\text{MSE}_{\eta,n}(k+1) - \text{MSE}_{\eta,n}(k) &\leq -C_1(\gamma, \gamma_0)\eta + \frac{C_1(\gamma, \gamma_0)\eta}{4} + 16e^{-N^*} \\
&= -\frac{C_1(\gamma, \gamma_0)\eta}{2} < 0.
\end{aligned}$$

□

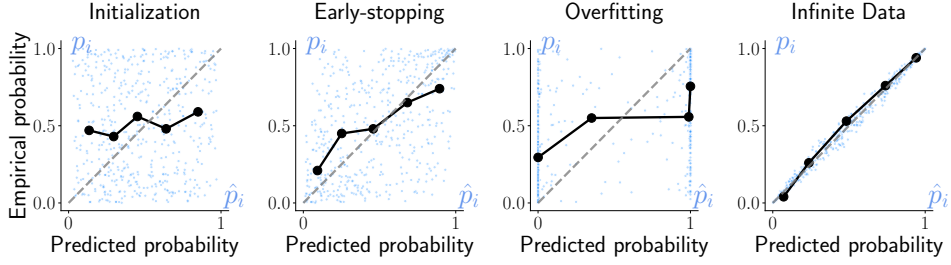


Figure 7: **Reliability curves for a linear model (Appendix B).** The horizontal and vertical coordinate of each blue point represent the predicted (\hat{p}_i) and true (p_i) probabilities of a test example respectively. We also show a reliability diagram of binned mean predicted and empirical probabilities in black (see Section 3). The dashed diagonal line indicates perfect calibration. The model is initialized randomly (first column) and initially improves the estimation, with the reliability curve trending towards the diagonal line (second column). However, because the dataset is finite, it eventually overfits, and the predicted probabilities collapse to 0 or 1 (third column). When labels are resampled to generate infinite data, the estimates converge to the ground-truth probability labels (right column).

B EARLY LEARNING AND MEMORIZATION

We provide a numerical example that illustrates the theoretical results of Section 4, and demonstrates the similarities between the behavior of linear and deep-learning models in high dimensions.

We train a logistic regression model in an overparametrized regime ($\frac{p}{n} = 1$). To generate the features, we draw $\{\mathbf{x}_i\}_{i=1}^{500}$, $\mathbf{x}_i \in \mathbb{R}^{500}$ i.i.d. Gaussian random variables, $\mathbf{x}_i \sim \mathcal{N}(0, I_{500})$. The ground-truth unobserved probability labels p_i are generated according to equation 6. i.e. $p_i = \sigma(\langle \boldsymbol{\theta}^*, \mathbf{x}_i \rangle)$. The true parameter $\boldsymbol{\theta}^* = (1, 0, \dots, 0)$ is fixed to equal the first standard basis vector, and $\sigma(x) = (1 + e^x)^{-1}$ is the sigmoid function.

The 0-1 labels $\{y_i\}_{i=1}^{500}$ are drawn from Bernoulli distribution with probability p_i , $y_i \sim \text{Bern}(p_i)$.

We use stochastic gradient descent (to fit a logistic regression model with parameter $\boldsymbol{\theta} \in \mathbb{R}^{500}$ on the simulated data $\{(\mathbf{x}_i, y_i)\}_{i=1}^{500}$, using a cross-entropy loss function. We compare the model trained on two datasets: (a) finite (\mathbf{x}, y) pairs, and (b) an infinite data set, generated by repeatedly resampling new outcomes y_i from the ground-truth probabilities p_i at every iteration.

Figure 7 shows that the linear model trained with cross entropy begins by improving the estimate of the true probabilities (at the early-learning stage), but eventually memorizes the 0-1 labels (the overfitting stage). Figure 8 illustrates that the MSE_p of cross entropy training increases when the model starts memorizing the 0-1 labels, as predicted by the results of Appendix A.

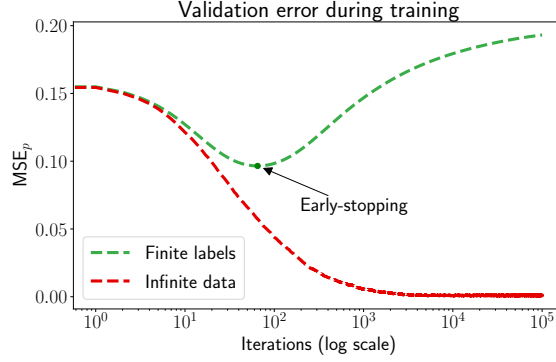


Figure 8: **Validation loss for training a linear model (Appendix B).** Training with finite data (green line) decreases MSE_p initially but eventually overfits to the 0-1 labels. Training with resampled labels (red line) avoids overfitting and results in accurate estimation of the true probabilities.

C ADDITIONAL RESULTS

We present here supplementary results to the ones presented in Section 8.

C.1 FACE-BASED RISK PREDICTION

Full evaluation with confidence intervals derived using 1000 bootstraps for the five simulated scenarios are examined: *Linear* (Table.3); *Sigmoid* (Table.4); *Centered* (Table.5); *Skewed* (Table.6); *Discrete* (Table.7). Note that all numbers are downscaled by 10^{-2} in the tables.

<i>Linear</i>	ECE	MCE	KS	Brier	MSE_p	KL_p
Infinite Data	4.14±0.81	12.07±3.29	2.24±0.88	18.97±0.33	1.14±0.04	2.82±0.11
CE early-stop	12.32±0.83	21.79±1.97	12.16±0.83	21.82±0.51	4.21±0.15	10.94±0.36
Temperature	5.7±0.74	13.82±2.71	2.36±0.74	20.47±0.37	2.73±0.11	6.75±0.25
Platt Scaling	4.29±0.77	10.94±2.55	1.3±0.45	20.18±0.36	2.48±0.09	6.07±0.22
Dirichlet Cal.	7.38±1.12	22.58±7.24	3.78±0.46	21.32±0.33	3.56±0.13	9.08±0.29
Focal Loss	5.34±0.68	13.31±2.67	3.56±0.85	21.99±0.28	4.13±0.11	10.52±0.28
Mix-n-match	5.46±0.84	12.9±2.51	1.92±0.44	20.43±0.35	2.7±0.11	6.72±0.24
Entropy Reg.	5.7±0.74	13.52±1.67	4.94±0.9	20.42±0.3	2.58±0.09	6.65±0.21
MMCE Reg.	4.89±0.74	12.57±2.27	1.92±0.46	20.04±0.38	2.24±0.08	5.68±0.2
Deep Ensemble	4.26±0.72	11.33±2.38	1.95±0.61	19.88±0.32	1.9±0.07	4.55±0.18
CaPE (bin)	4.58±0.75	11.85±2.49	1.71±0.51	19.68±0.36	1.78±0.07	4.35±0.16
CaPE (kernel)	4.62±0.62	12.25±2.31	1.65±0.38	19.71±0.34	1.74±0.07	4.3±0.17

Table 3: Performance on Face-based Risk Prediction. *Linear* scenario.

<i>Sigmoid</i>	ECE	MCE	KS	Brier	MSE _p	KL _p
Infinite Data	6.4±0.71	20.63±3.44	2.74±0.45	16.28±0.44	5.34±0.2	14.82±0.51
CE early-stop	6.19±0.75	17.0±3.68	5.86±0.8	16.68±0.42	6.16±0.17	17.16±0.48
Temperature	5.57±0.71	15.32±3.09	5.02±0.83	16.58±0.34	6.13±0.17	17.09±0.43
Platt Scaling	3.45±0.68	10.32±2.79	1.3±0.43	16.33±0.34	5.78±0.19	16.15±0.47
Dirichlet Cal.	14.5±1.15	25.68±3.02	4.67±0.32	19.21±0.43	8.64±0.26	25.18±0.58
Focal Loss	4.65±0.7	11.84±2.78	2.66±0.77	16.96±0.34	6.86±0.21	19.46±0.5
Mix-n-match	5.65±0.76	15.32±3.41	5.09±0.94	16.6±0.36	6.12±0.17	17.08±0.46
Entropy Reg.	9.51±0.79	18.77±2.38	7.26±0.78	17.17±0.31	7.02±0.17	21.16±0.42
MMCE Reg.	4.67±0.76	13.63±2.59	2.5±0.53	15.9±0.51	5.35±0.18	15.06±0.49
Deep Ensemble	5.17±0.74	16.12±3.11	2.04±0.44	16.39±0.45	5.86±0.22	16.46±0.6
CaPE (bin)	3.78±0.6	11.96±2.59	2.22±0.7	15.84±0.43	5.17±0.2	14.27±0.49
CaPE (kernel)	3.9±0.75	11.73±2.79	2.05±0.54	15.85±0.41	5.16±0.2	14.34±0.49

Table 4: Performance on Face-based Risk Prediction. *Sigmoid* scenario.

<i>Centered</i>	ECE	MCE	KS	Brier	MSE _p	KL _p
Infinite Data	4.29±0.74	12.38±2.92	2.68±0.8	24.22±0.13	0.2±0.01	0.41±0.01
CE early-stop	5.76±0.84	15.32±3.07	4.19±1.02	24.68±0.08	0.48±0.01	0.98±0.03
Temperature	6.09±0.82	15.83±2.91	4.74±0.96	24.74±0.06	0.48±0.01	0.98±0.03
Platt Scaling	4.57±0.76	11.85±2.5	2.79±0.85	24.62±0.08	0.41±0.01	0.83±0.03
Dirichlet Cal.	4.84±1.15	13.13±7.61	2.16±0.86	24.7±0.1	0.46±0.01	0.94±0.03
Mix-n-match	6.05±0.83	15.71±2.92	4.68±0.98	24.74±0.06	0.48±0.01	0.98±0.02
Focal Loss	5.09±0.83	13.4±2.87	3.44±1.02	24.8±0.05	0.48±0.01	0.97±0.03
Entropy Reg.	5.02±0.86	12.69±3.42	3.27±0.96	24.74±0.06	0.45±0.01	0.92±0.03
MMCE Reg.	5.56±0.86	13.59±2.65	2.71±0.93	24.7±0.08	0.44±0.01	0.9±0.03
Deep Ensemble	4.84±0.78	12.39±2.52	2.64±0.71	24.69±0.07	0.44±0.01	0.89±0.03
CaPE (bin)	4.73±0.82	11.81±2.54	2.07±0.6	24.56±0.11	0.38±0.01	0.78±0.03
CaPE (kernel)	5.41±0.87	12.71±2.5	2.39±0.78	24.59±0.11	0.4±0.01	0.81±0.03

Table 5: Performance on Face-based Risk Prediction. *Centered* scenario.

<i>Skewed</i>	ECE	MCE	KS	Brier	MSE _p	KL _p
Infinite Data	2.7±0.46	7.64±2.14	1.05±0.39	11.0±0.51	0.22±0.01	0.92±0.03
CE early-stop	3.07±0.57	7.88±1.88	1.28±0.41	11.18±0.5	0.4±0.01	1.79±0.06
Temperature	3.14±0.49	7.92±1.84	1.12±0.33	11.22±0.47	0.4±0.02	1.76±0.06
Platt Scaling	2.99±0.53	7.73±1.59	1.07±0.37	11.1±0.54	0.39±0.01	1.72±0.06
Dirichlet Cal.	3.04±0.73	7.81±2.43	0.97±0.3	11.22±0.42	0.47±0.02	2.31±0.07
Focal Loss	8.29±0.67	14.93±1.43	6.16±0.67	12.01±0.41	1.28±0.03	1.63±0.66
Mix-n-match	2.99±0.53	7.78±1.78	1.08±0.32	11.18±0.49	0.4±0.01	1.75±0.05
Entropy Reg.	7.67±0.57	14.43±1.5	5.2±0.71	11.94±0.45	1.18±0.03	10.74±0.65
MMCE Reg.	3.68±0.59	10.94±2.76	1.47±0.31	11.14±0.44	0.54±0.02	2.44±0.08
Deep Ensemble	2.87±0.5	7.21±1.63	1.36±0.44	11.28±0.5	0.55±0.02	2.58±0.07
CaPE (bin)	3.29±0.5	8.18±1.51	1.17±0.34	11.07±0.47	0.4±0.02	1.73±0.06
CaPE (kernel)	3.16±0.5	8.14±1.58	1.09±0.33	11.17±0.53	0.39±0.01	1.69±0.06

Table 6: Performance on Face-based Risk Prediction. *Skewed* scenario.

<i>Discrete</i>	ECE	MCE	KS	Brier	MSE _p	KL _p
Infinite Data	4.23±0.74	11.16±2.5	1.45±0.49	20.38±0.35	1.52±0.05	3.63±0.12
CE early-stop	6.7±0.86	18.62±3.52	2.61±0.53	21.91±0.36	2.24±0.08	5.27±0.17
Temperature	6.12±0.87	16.82±3.56	3.37±0.86	21.76±0.35	2.21±0.08	5.15±0.18
Platt Scaling	4.7±0.72	11.69±2.44	1.67±0.51	21.44±0.32	2.06±0.08	4.83±0.17
Dirichlet Cal.	7.13±0.86	22.67±5.08	3.18±0.68	22.1±0.34	2.74±0.1	6.53±0.22
Focal Loss	5.7±0.75	13.68±2.32	4.62±0.91	21.77±0.28	2.92±0.09	6.77±0.21
Mix-n-match	6.27±0.76	16.83±2.95	3.47±0.93	21.77±0.33	2.21±0.08	5.14±0.18
Entropy Reg.	6.69±0.87	15.38±2.43	6.03±1.13	21.79±0.31	2.84±0.08	6.62±0.19
MMCE Reg.	3.96±0.7	10.4±2.4	1.51±0.47	21.12±0.35	2.09±0.08	4.92±0.18
Deep Ensemble	4.76±0.74	11.49±2.23	2.04±0.61	21.17±0.31	1.97±0.08	4.61±0.17
CaPE (bin)	5.41±0.74	14.45±3.15	2.24±0.59	21.33±0.36	1.81±0.08	4.28±0.18
CaPE (kernel)	4.96±0.8	12.97±2.63	2.18±0.58	21.21±0.42	1.84±0.08	4.35±0.17

Table 7: Performance on Face-based Risk Prediction. *Discrete* scenario.

C.2 SUPPLEMENTARY METRICS ON REAL-WORLD DATASET

We present here additional metrics on the real world data: Cancer Survival (Table 8); Climate Forecasting (Table 9); Collision Prediction (Table 10).

Methods	($\times 10^{-2}$)	AUC	ECE	MCE	NLL	Brier	KS
CE Early-stop		58.88	12.25	25.35	67.92	23.96	6.44
Temperature		58.88	12.07	24.65	67.11	23.73	6.92
Platt Scaling		58.91	10.28	27.69	66.11	23.33	4.91
Dirichlet Cal.		49.89	13.83	35.52	67.57	24.08	6.00
Mix-n-match		58.88	12.16	24.52	66.89	23.67	7.18
Focal loss		55.02	12.15	26.34	65.92	23.31	6.38
Entropy Reg.		56.29	11.73	30.81	66.49	23.62	6.83
MMCE Reg.		48.45	11.84	37.36	66.83	23.73	3.64
Deep Ensemble		52.26	9.99	28.30	66.22	23.47	5.02
CaPE (bin)		61.44	12.31	25.27	65.75	23.20	2.59
CaPE (kernel)		61.22	9.48	32.40	65.70	23.18	3.70

Table 8: Baselines with full metrics for cancer survival

Methods	($\times 10^{-2}$)	AUC	ECE	MCE	NLL	Brier	KS
CE Early-stop		77.64	10.91	25.50	59.97	20.57	11.03
Temperature		77.64	8.66	23.56	58.77	20.21	7.41
Platt Scaling		77.65	6.97	16.47	57.38	19.53	3.26
Dirichlet Cal.		77.51	14.29	30.09	62.83	21.89	5.21
Mix-n-match		77.64	8.65	23.58	58.77	20.21	7.39
Focal Loss		76.18	8.32	21.25	59.01	20.27	4.45
Entropy Reg		79.01	10.53	20.72	57.83	19.77	5.00
MMCE Reg		76.69	8.46	19.73	59.25	20.12	7.31
Deep Ensemble		79.86	7.41	18.24	55.28	18.82	7.57
CaPE (bin)		78.99	5.16	15.09	79.00	18.37	2.34
CaPE (kernel)		79.00	5.08	13.28	54.32	18.39	2.34

Table 9: Baselines with full metrics for weather prediction

Methods	($\times 10^{-2}$)	AUC	ECE	MCE	NLL	Brier	KS
CE Early-stop		85.68	4.36	19.87	31.67	8.59	1.54
Temperature		85.68	4.56	16.79	30.36	8.52	2.9
Platt Scaling		85.76	3.04	12.39	29.42	8.23	1.52
Dirichlet Cal.		83.36	5.78	18.13	30.90	8.77	1.60
Mix-n-match		85.68	4.40	17.41	30.25	8.52	2.60
Focal Loss		82.21	9.07	19.85	34.41	9.82	8.72
Entropy Reg		83.15	14.54	21.27	38.74	11.10	13.44
MMCE Reg.		85.18	2.94	8.95	30.65	8.48	2.44
Deep Ensemble		85.27	3.15	16.53	30.20	8.54	2.01
CaPE (bin)		85.70	3.16	12.21	30.61	8.18	2.13
CaPE (kernel)		85.95	3.22	13.32	30.44	8.13	2.10

Table 10: Baselines with full metrics for collision prediction

C.3 ADDITIONAL RELIABILITY DIAGRAM

We present here additional reliability curves to the ones illustrated in Figure 6 We present here additional reliability curves for the different synthetic data scenarios, mentioned in Figure 4.

D KOLMOGOROV-SMIRNOV ERROR

We derive the KS-error, mentioned in Section 3.

For a calibrated estimator

$$\mathbb{P}(y = 1 | f(\mathbf{x}) \in I(q)) = q, \quad \forall 0 \leq q \leq 1,$$

for some small interval $I(q)$ around q .

Hence

$$\mathbb{P}(y = 1, f(\mathbf{x}) \in I(q)) = \mathbb{P}(f(\mathbf{x}) \in I(q)) q, \quad \forall 0 \leq q \leq 1$$

. Similarly to the Kolmogorov-Smirnov (KS) test for distribution functions, we can recast this property in integral form

$$\phi_1(\sigma) = \int_0^\sigma \mathbb{P}(y = 1, f(\mathbf{x}) \in I(q)) dq, \quad \phi_2(\sigma) = \int_0^\sigma \mathbb{P}(f(\mathbf{x}) \in I(q)) q dq$$

We can evaluate ϕ_1, ϕ_2 from a finite sample $(\mathbf{x}_i, y_i), i = 1 \dots n$,

$$\phi_1(\sigma) = \frac{1}{n} \sum_{i=1}^n \mathbf{1}(y_i = 1, f(\mathbf{x}_i) \leq \sigma), \quad \phi_2(\sigma) = \frac{1}{n} \sum_{i=1}^n \mathbf{1}(f(\mathbf{x}_i) \leq \sigma) f(\mathbf{x}_i)$$

The KS error is defined as

$$\text{KS} = \max_{1 \leq \sigma \leq 1} |\phi_1(\sigma) - \phi_2(\sigma)|$$

ϕ_1, ϕ_2 can be efficiently computed by sorting the data points with respect to their confidence scores $f(\mathbf{x}_i)$. The KS error has the advantage of being independent of binning configurations, unlike ECE and MCE.

E BRIER SCORE DECOMPOSITION

We present here a decomposition of the Brier score into two components, discussed in Section 3.

The Brier score can be interpreted as a sum of two terms, calibration and refinement. Assume the network can output one of K distinct possible predictions, i.e., $\hat{p} \in \{\hat{q}_1, \dots, \hat{q}_K\}$.

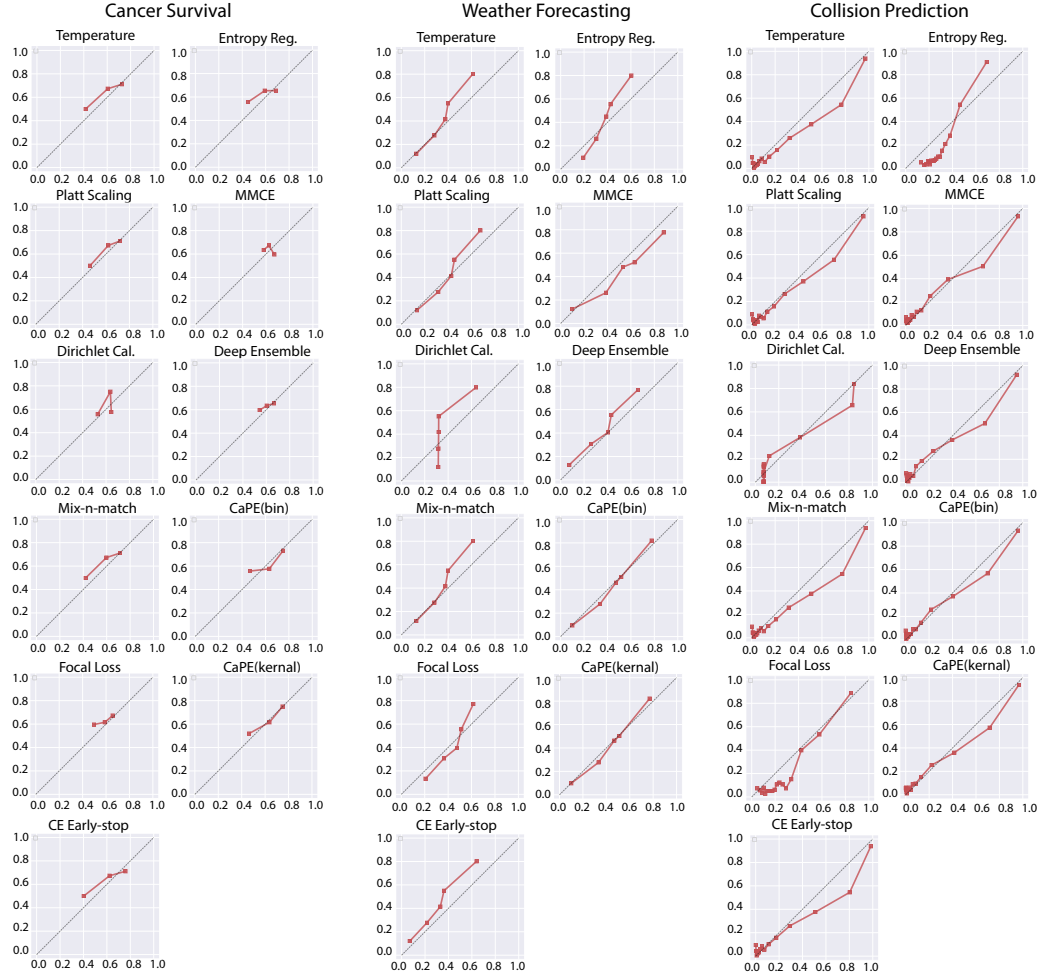


Figure 9: Reliability diagrams of all the baselines on real-world datasets. We train all baseline methods on each of the datasets and plot the empirical probability(y-axis) against predicted probability(x-axis). The axis labels are removed due to space constraints.

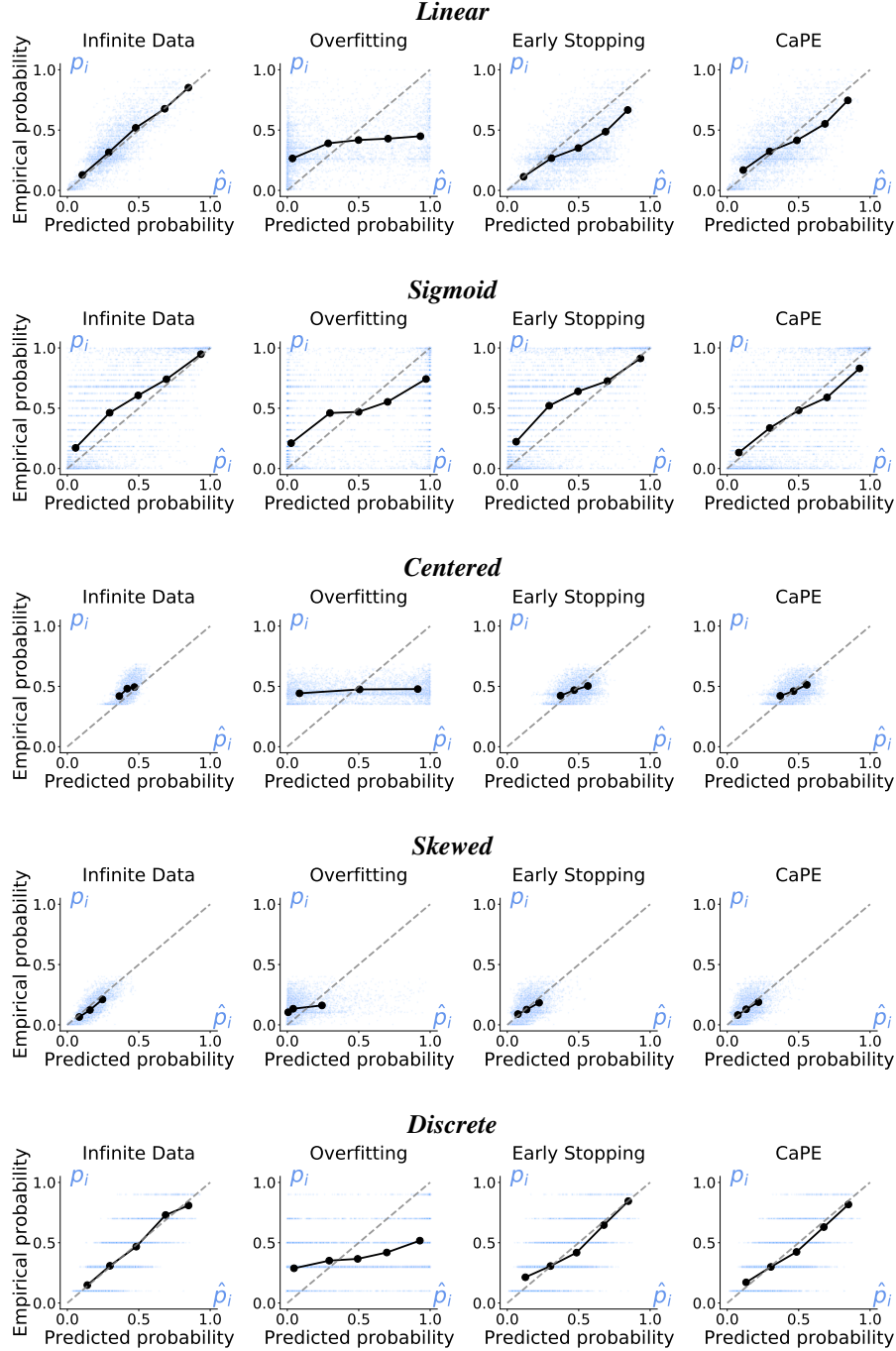


Figure 10: Reliability diagrams for different synthetic data scenarios. We can see that CaPE outperforms early stopping, prevents overfitting, and achieves a performance on par with training on infinite resampled data.

Denote S_k , the set of all inputs with output p_k and \bar{q}_k the empirical probability over S_k , i.e.,

$$S_k = \{\mathbf{x} | f(\mathbf{x}) = \hat{q}_k\}, \quad |S_k| = n_k, \quad \bar{q}_k = \frac{1}{n_k} \sum_{\mathbf{x}_i \in S_k} y_i$$

Then we can write

$$\text{Brier} = \frac{1}{N} \sum_{i=1}^N (\hat{p}_i - y_i)^2 = \frac{1}{N} \sum_{k=1}^K n_k (\hat{q}_k - \bar{q}_k)^2 + \frac{1}{N} \sum_{k=1}^K n_k \bar{q}_k (1 - \bar{q}_k),$$

The first term on the RHS, calibration, is similar to MSE_p , with the empirical probabilities \bar{q}_k substituting for the true labels. The second term, refinement, is an estimate of the confidence in determining \bar{q}_k . It is related to the area under curve (AUC), which measures to the achievable accuracy of the network as a classifier. The term is smaller as the prediction classes \bar{q}_k tend towards 0 or 1. Thus, this term penalizes empirically calibrated predictors, with low discriminative power, as in Figure 2.

F METRIC COMPARISON

We present here the correlation between different calibration and accuracy metrics and metrics that have access to the ground truth probabilities, MSE_p and KL-divergence, evaluated over all five scenarios in our Face-based Risk Prediction synthetic dataset, referred to in Section 3.

G ESTIMATION OF EMPIRICAL PROBABILITY IN CAPE

We describe in further detail the two ways to estimate the conditional probability $\mathbb{P}(y = 1 | f(\mathbf{x}) \in I(q))$, introduced in Section 5.

We wish to estimate the conditional probability of an output y given a network prediction $f(\mathbf{x})$, $\mathbb{P}(y = 1 | f(\mathbf{x}) \in I(q))$. We can approximate the probability by averaging over points $\hat{p} \in I(q)$,

$$\mathbb{P}(y = 1 | f(\mathbf{x}) \in I(q)) \approx \frac{1}{|I(q)|} \sum_{\hat{p} \in I(q)} \mathbb{P}(y = 1 | f(\mathbf{x}) = \hat{p}) \quad (17)$$

An empirical estimate of $\mathbb{P}(y = 1 | f(\mathbf{x}) \in I(q))$ would be

$$\mathbb{P}(y = 1 | f(\mathbf{x}) \in I(q)) \approx \frac{1}{|\text{Index}(I(q))|} \sum_{f(\mathbf{x}_i) \in I(q)} y_i, \quad (18)$$

where $\text{Index}(I_q) = \{i | f(\mathbf{x}_i) \in I(q)\}$.

Alternatively, we can use kernel estimation:

$$\mathbb{P}(y = 1 | f(\mathbf{x}) \in I(q)) \approx \frac{1}{Z} \sum_{\hat{p} \in I(q)} \mathbb{P}(y = 1 | f(\mathbf{x}) = \hat{p}) \cdot \exp\left(-\frac{(p-q)^2}{\sigma^2}\right), \quad (19)$$

where $Z = \sum_{p \in I(q)} \exp\left(-\frac{(p-q)^2}{\sigma^2}\right)$ is the normalization factor. An empirical estimate of the conditional probability would then be

$$\mathbb{P}(y = 1 | f(\mathbf{x}) \in I(q)) \approx \frac{1}{Z} \sum_{f(\mathbf{x}_i) \in I(q)} y_i \exp\left(-\frac{(f(\mathbf{x}_i) - q)^2}{\sigma^2}\right). \quad (20)$$

Based on these two approximation methods, we can design an algorithm to estimate p_{emp}^i .

Bin We divide our data into B bins of equal size. Q_1, \dots, Q_B are the data B-quantiles. We wish to estimate $\mathbb{P}(y = 1 | f(\mathbf{x}) \in [Q_{b-1}, Q_b])$, $b = 1, \dots, B$, $Q_0 = 0$. Denote $I_b := [Q_{b-1}, Q_b] \cap \{f(\mathbf{x}_i)\}_{i=1}^N$, set of all predictions in $[Q_{b-1}, Q_b]$, and $\text{Index}(I_b) = \{i | f(\mathbf{x}_i) \in I_b\}$. We have,

$$\mathbb{P}(y = 1 | f(\mathbf{x}) \in [Q_{b-1}, Q_b]) \approx p_{\text{emp}}^{(b)} = \frac{1}{|I_b|} \sum_{i \in \text{Index}(I_b)} y_i$$

We assign $p_{\text{emp}}^{(b)}$ to all data points i in the b -th quantile

$$p_{\text{emp}}^i = p_{\text{emp}}^{(b)} \quad \forall i \in \text{Index}(I_b)$$

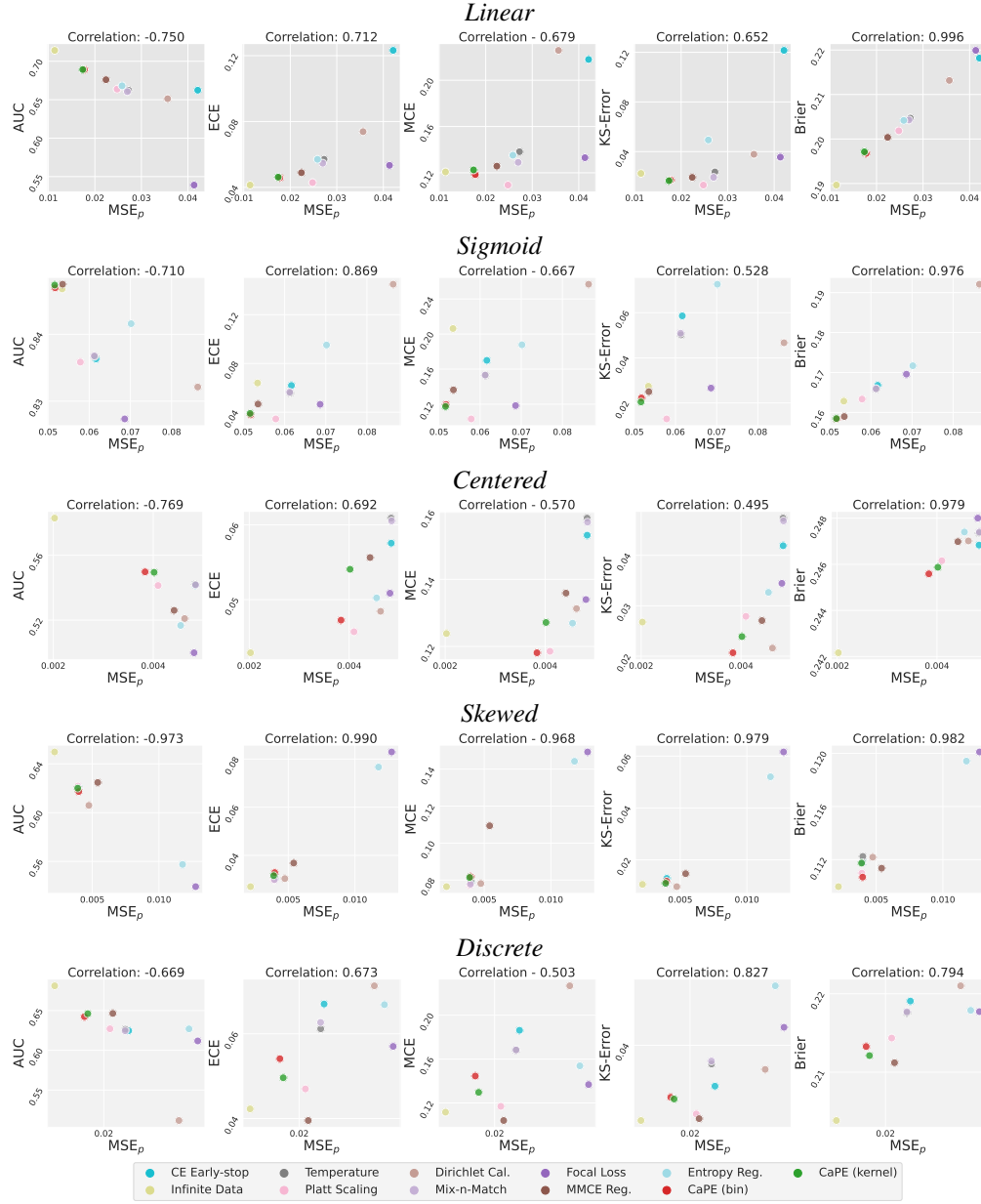


Figure 11: Comparison between MSE_p and other metrics on synthetic data. Brier score presents the most consistent correlation with MSE_p .



Figure 12: Comparison between KL_p and other metrics on synthetic data. Brier score presents the most consistent correlation with KL_p .

Kernel In this case we use kernel estimation:

$$p_{\text{emp}}^i = \frac{\sum_{k \in \text{NN}(i, r)} K(i, k) y_k}{\sum_{k \in \text{NN}(i, r)} K(i, k)}. \quad (21)$$

$\text{NN}(i, r)$ defines r data points whose predictions are nearest to $\hat{p}_i = f(\mathbf{x}_i)$. $K(i, j)$ is the Gaussian kernel

$$K(i, j) = \exp\left(-\frac{(\hat{p}_i - \hat{p}_j)^2}{\sigma^2}\right),$$

with hyperparameter σ .

H CALIBRATION BASELINES

This section includes a review of the baseline methods, discussed in Section 7

Post-processing Postprocessing for calibration requires finding a function $f : [0, 1] \rightarrow [0, 1]$, that augments the output of a the neural network $\hat{p}_i \rightarrow f(\hat{p}_i)$ in order to achieve better calibration properties

- Platt scaling (Platt, 1999) optimizes f on validation set within the following family,

$$f_1(\hat{p}_i) = \sigma(W^T \hat{p}_i + b) \quad (22)$$

where $W \in \mathbb{R}^2$, $b \in \mathbb{R}$ and σ is the Sigmoid function. The non-probabilistic predictions of a classifier are used as features for a logistic regression model, which is trained on the validation set to return probabilities.

- Temperature scaling (Guo et al., 2017) is a single parameter variant of Platt Scaling where we only change the temperature of the softmax to obtain the calibrated probabilities.

$$f(\hat{p}_i) = \text{Softmax}(\hat{p}_i/T) \quad (23)$$

where $T \in \mathbb{R}$ minimizes the negative log-likelihood of validation set.

- Beta/Dirchlet calibration (Dir-ODIR) (Kull et al., 2017; 2019) assumes that the probabilities can be parametrized by a Beta/Dirchlet distribution i.e.

$$f_j \sim \text{Beta}(\alpha^{(j)}, \beta^{(j)}) \quad (24)$$

Assume the prior to be $p(y = j) = \pi_j$, $\pi_j \in [0, 1]$, we have $P(y|f_j) \propto \pi_j f_j$, and then $\alpha^{(j)}, \beta^{(j)}$ are estimated by maximizing the posterior.

Ensembling These calibration methods simultaneously train several neural networks from end to end, varying parameters in the training process. The final output is some function of all the different outputs.

- Mix-n-Match (Zhang et al., 2020) improves calibration by ensembling parametric and non-parametric calibrators. Denote the temperature scaling function with $g(\hat{y}_i, T)$. Then Mix-n-Match ensembles different temperatures

$$f_j(\hat{p}_i) = w_1 g_j(\hat{p}_i, T) + w_2 g_j(\hat{p}_i, 0) + w_3 g_j(\hat{p}_i, \infty) \quad (25)$$

After ensembling the parametric temperature scaling, Mix-n-Match applies non-parametric isotonic regression.

- Deep ensemble (Lakshminarayanan et al., 2017) trains M copies of the neural network with different initialization. The probability estimation is the average of all single model estimations

$$p(y_i | x_i) = \frac{1}{M} \sum_j^M p_{\theta_j}(y_i | x_i) \quad (26)$$

Modified training These calibration methods train the neural networks from end to end, modifying the training process to improve calibration.

- Confidence penalty (Pereyra et al., 2017) Penalizes low entropy output distributions (confidence penalty). Label smoothing improve state-of-the-art models across benchmarks.

$$\mathcal{L}(\theta) = - \sum_i \log p_\theta(y_i|x_i) - \beta H(p_\theta(y_i|x_i)) \quad (27)$$

- Focal loss (Mukhoti et al., 2020) maximizes entropy while minimizing the KL divergence between the predicted and the target distributions. It also regularizes the weights of the model to avoid overfitting.

$$\mathcal{L}(\theta) = - \sum_i (1 - p_\theta(y_i|x_i))^\gamma \log p_\theta(y_i|x_i), \quad \gamma \in \mathbb{R}. \quad (28)$$

- Kernel MMCE (Kumar et al., 2018) is a reproducing kernel Hilbert space (RKHS) kernel based measure of calibration that is efficiently trainable, alongside the negative likelihood loss. Given data samples $\mathcal{D} = \{(c_i, r_i)\}_{i=0}^m$, where $c_i = \chi_{\{\hat{y}_i=y_i\}}$ and $r_i = \mathbb{P}(c_i = 1|\hat{y}_i)$, MMCE is computed on samples \mathcal{D} as following,

$$\text{MMCE}^2(\mathcal{D}) = \sum_{i,j} \frac{(c_i - r_i)(c_j - r_j)k(r_i, r_j)}{m^2} \quad (29)$$

where $k(r_i, r_j)$ is a kernel function. MMCE is optimized together with the cross entropy loss as a regularization term. The strength of calibration can be adjusted by a scale $\lambda \in \mathbb{R}$.

$$\mathcal{L}(\theta) = - \sum_i \log p_\theta(y_i|x_i) + \lambda (\text{MMCE}^2(D))^{\frac{1}{2}} \quad (30)$$

I SYNTHETIC DATA EXPERIMENTS

We use ResNet-18 model for all our experiments with synthetic data.

The synthetic data is split into training, validation, and test sets with 16641, 4738, and 2329 samples, respectively. The training and validation sets contain only images x_i and 0-1 labels y_i for training and tuning the model. In order to evaluate the performance of the model for probability estimation, the held-out test set contains the ground truth probabilities p_i , in addition to x_i and y_i . Note that we do not use the ground-truth probability labels p_i values during training or inference - we only use them to compare the performance of different models.

Ground Truth Probability Generation The ground truth probability associated with example i is simulated by $p_i = \psi(z_i)$ where z_i is age of the person.

Label distribution After determining the probability p_i using $\psi(z)$, the label y_i is sampled from a Bernoulli distribution parametrized by p_i , so that it takes the value 1 with probability p_i . The distributions of y_i under five different scenarios are illustrated in Fig.14.

J REAL-WORLD DATA AND EXPERIMENT DETAILS

We present here supplementary information for the real-world datasets used in our experiments.

Cancer Survival Histopathological features are useful in identification of tumor cells, cancer subtypes, and the stage and level of differentiation of the cancer. Hematoxylin and Eosin (H&E)-stained slides are the most common type of histopathology data and the basis for decision making in the clinics. With these properties, H&E are used for mortality prediction of cancer (Wulczyn et al., 2020). In this experiment, we use the H&E slides of non-small cell lung cancers from The Cancer Genome Atlas Program (TCGA)⁶ to predict the 5-year survival. The dataset has 1512 whole slide images from 1009 patients, and 352 of them died in 5-years. We split the samples by patients and source institutions into training, validation, and test set, which has 1203, 151, and 158 samples respectively.

The whole slide images contain numerous pixels, so we cropped the slides into tiles at 20x magnification with 1/4 overlapping, resized them to 299×299 with bicubic interpolation, and filtered

⁶<https://www.cancer.gov/tcga>

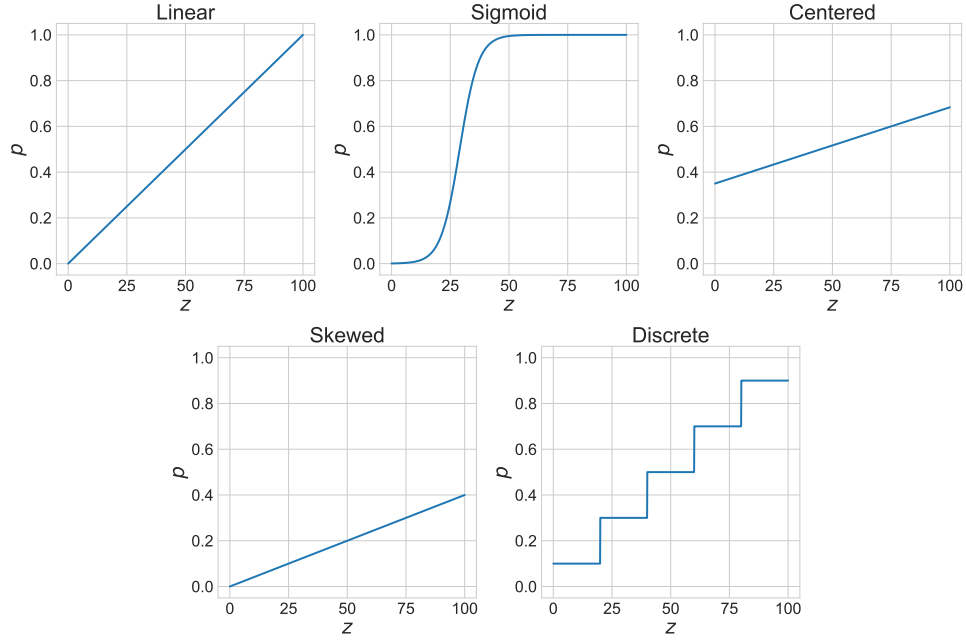


Figure 13: Illustration of the function $\psi(z)$ used to generate the different synthetic-data scenarios.

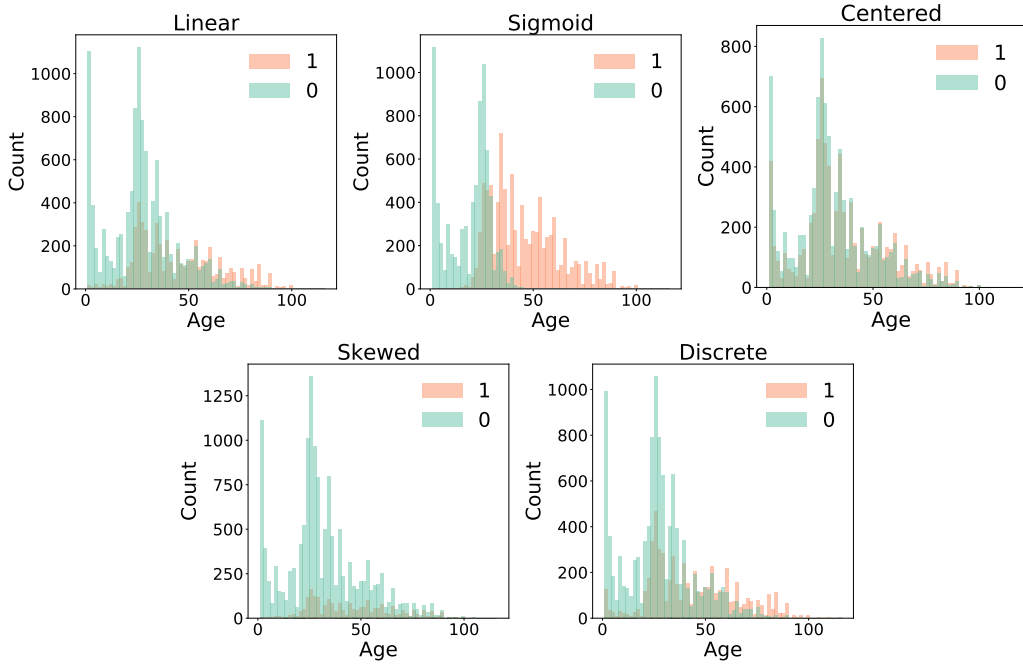


Figure 14: Histograms of the outcomes (y_i) for the different synthetic-data scenarios.

out the tiles with more than 85% area covered by the background. The representations of each tile are trained with self-supervised momentum contrastive learning (MoCo) (Chen et al., 2020), and the slide-level prediction is obtained from a multiple-instance learning network (Ilse et al., 2018) trained with the binary label of survival in 5 years.

Weather Forecasting We use the German Weather service dataset⁷, which contains quality-controlled rainfall-depth composites from 17 operational Doppler radars. Three precipitation maps from the past 30 minutes serve as an input. The training labels are the 0/1 events indicating whether the mean precipitation increases (1) or not (0).

The German Weather service (DWD - Deutscher Wetter Dienst) dataset <https://opendata.dwd.de/weather/radar/> contains quality-controlled rainfall-depth composites from 17 operational DWD Doppler radars. It has a spatial extent of 900x900 km, and covers the entirety of Germany. Data exists since 2006, with a spatial and temporal resolution of 1x1 km and 5 minutes, respectively. The dataset has been used to train RainNet, a precipitation nowcasting model (Ayzel, 2020).

The network architecture is ResNet18, with 3 input channels and 2 output channels. The input to the network are 3 precipitation maps which cover a fixed area of 300km×300 km in the center of the grid (300×300 pixels), set 10 minutes apart. The training, validation and test datasets consist of 20000, 6000 and 3000 samples, respectively, all separated temporally, over the span of 15 years.

Collision Prediction Vehicle collision is one of the leading causes of death in the world. Reliable collision prediction systems which can warn drivers about potential collisions can save a significant number of lives. A standard way to design such a system is to train a convolutional model for identifying if a particular vehicle in the dash-cam video feed might collide with the car in next few seconds. More formally, at time $t = T$ the system tries to predict if any car in the video might collide with our given car in time $t \in [T, T + T_{\text{look-ahead}}]$. Each labelled training sample consists of features $X = (X^{T-\delta}, X^{T-2\delta}, \dots, X^{T-d\delta})$ and a binary label $Y \in \{0, 1\}$ denoting if an accident will occur in $t \in [T, T + T_{\text{look-ahead}}]$. Each X^t is a tensor with 4 channels where the first 3 channels corresponds to an RGB image of the dashcam view at time $t = t$, and the fourth channel consists of a mask with a bounding box on a particular vehicle of interest. In this work, we use *YouTubeCrash* dataset (Kim et al., 2019) to train and test our model, which uses $\delta = 0.1s, T_{\text{look-ahead}} = 18\delta = 1.8s$, and $d = 3$. Following Kim et al. (2019) we used a VGG-16 network architecture.

The dataset contains 122 accident scenes, and 2096 non-accident scenes, which after feature extraction gives us 2096 positive samples, and 11486 negative samples (the dataset is severely imbalanced, and similar to the Skewed situation in Section 7.1). We further split the dataset into train (6453 samples for label 0, and 1023 samples for label 1), validation (2348 samples for label 0, and 545 samples for label 1), and test (2685 samples for label 0, and 528 samples for label 1) sets. The samples in train, validation and test sets are generated from disjoint scenes/dashcam videos.

K ANALYSIS OF CANCER SURVIVAL RESULTS

For cancer survival prediction, we visualize the estimated probabilities on the test set in different pathological stages in Figure 15. In general, patients in earlier stages should have higher probabilities of survival. Deep ensemble produces similar probability estimates for all stages (i.e the model is less discriminative). Cross-entropy minimization (CE) is more discriminative, but has very wide confidence intervals. CaPE is more discriminative than deep ensemble, while having narrower confidence intervals than CE.

L CALIBRATING FROM THE BEGINNING

CaPE exploits a calibration-based cost function to improve its probability estimates without overfitting. The empirical probabilities in this loss are computed from the model itself. Consequently, applying this strategy from the beginning of training can be counterproductive, because the model predictions are essentially random. This is demonstrated in the following table, which compares CaPE with a model trained using the calibration loss from the beginning (in the same way as CaPE, alternating with cross-entropy minimization).

⁷<https://opendata.dwd.de/weather/radar/>

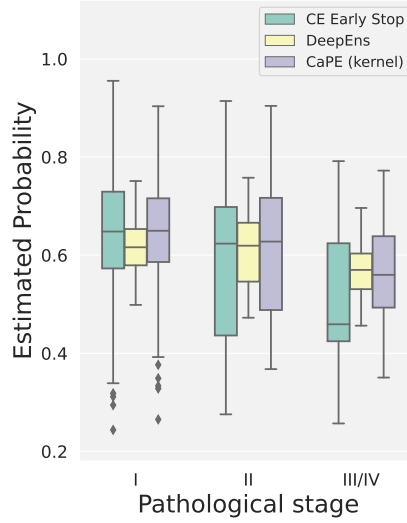


Figure 15: Estimated probability of survival grouped by pathological stages. The plot shows median, samples between 25th to 75th percentile in the box, samples between 0th and 100th percentile on the line, and the outliers as dots. Deep ensemble produces similar probability estimates for patients across all the stages; CE is more discriminative but has a very large variance; CaPE achieves a trade-off between the two baselines.

Methods ($\times 10^{-2}$)	<i>Linear</i>		<i>Sigmoid</i>		<i>Centered</i>		<i>Skewed</i>		<i>Discrete</i>	
	MSE_p	KL_p	MSE_p	KL_p	MSE_p	KL_p	MSE_p	KL_p	MSE_p	KL_p
Bin (start)	2.59	6.81	8.07	22.10	0.48	0.98	0.51	2.37	2.74	6.36
Kernel (start)	2.23	5.68	7.60	21.15	0.54	1.10	0.68	2.84	2.40	5.63
Bin (CaPE)	1.83	4.46	5.29	14.59	0.38	0.78	0.40	1.72	1.83	4.31
Kernel (CaPE)	1.81	4.41	5.22	14.47	0.40	0.81	0.39	1.70	1.85	4.36

Table 11: Comparison between CaPE and a model that uses the calibration loss from the beginning (in the same way as CaPE, alternating with cross-entropy minimization) on synthetic data.

M COMPARISON OF REAL-WORLD DATASETS WITH DIFFERENT SCENARIOS OF THE SIMULATED DATASET

Figure 16 illustrates the similarity between the empirical probability curves of different real-world datasets and the different scenarios of our synthetic dataset. For the cancer survival dataset, the empirical probabilities are clustered in the center (0.4-0.6) similar to the *Centered* scenario. For the weather forecasting dataset, the probabilities are uniformly distributed across 0.1-0.8 similar to the *Linear* scenario. For the collision prediction dataset, the majority of the data points are clustered in the lower probability region which makes it similar to the *Skewed* scenario.

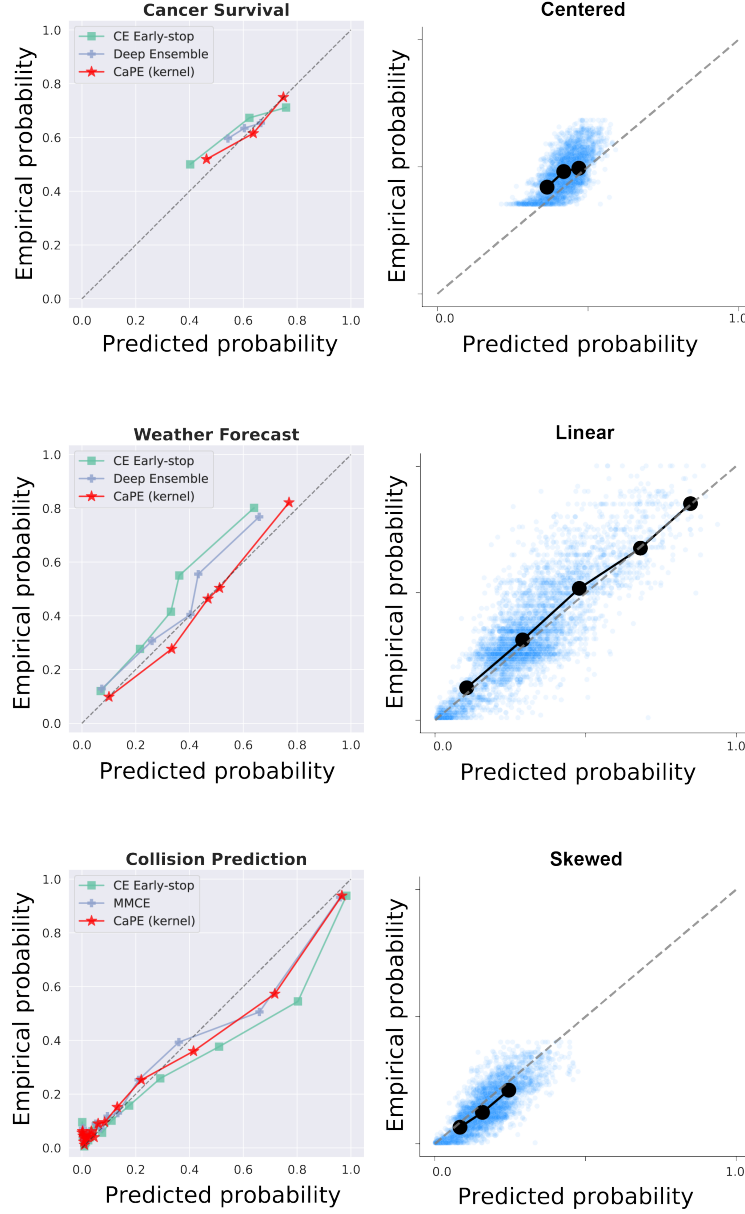


Figure 16: **Comparison of reliability diagrams for real-world data with different scenarios of simulated data.** For the cancer survival dataset, the empirical probabilities are clustered in around (0.4-0.6), similar to the *Centered* scenario. For the weather forecasting dataset, the probabilities are uniformly distributed across 0.1-0.8, similar to the *Linear* scenario. For the collision prediction dataset, the majority of the output probabilities are clustered in the lower probability region, similar to the *Skewed* scenario.